A DROPLET-BASED MICROFLUIDIC IMPEDANCE FLOW CYTOMETER FOR DETECTION AND QUANTIFICATION OF MICROPLASTICS IN WATER

by

Mohammadreza Aghel

B.Sc., Iran University of Science and Technology, 2019

A THESIS SUBMITTED IN PARTIAL FULFILLMENT OF

THE REQUIREMENTS FOR THE DEGREE OF

MASTER OF APPLIED SCIENCE

in

THE FACULTY OF GRADUATE STUDIES

(Department of Mechanical Engineering)

University of Victoria

Supervisory Committee

Mina Hoorfar, Department of Mechanical Engineering

Supervisor

Mohsen Akbari, Department of Mechanical Engineering

Supervisory Committee Member

Abstract

The purpose of this thesis is to design and test a new microfluidic device based on impedance cytometry principles for detecting and quantifying microplastics in droplets. To measure the size and concentration of microplastics, we created a flow-focusing droplet generator with coplanar electrodes. Polystyrene microbeads of four distinct sizes and three different concentrations were employed. The impedance measurements were taken with a lock-in amplifier at three distinct frequencies: 4.4 MHz, 11 MHz, and 22.5 MHz. ANOVA and k-NN classification were used to examine the findings. The signal phase at low and medium frequencies was proven to best differentiate between different sizes and concentrations. The functional groups (for example, carboxyl groups) on the surface of microplastics can significantly interfere with the signal phase. The ANOVA and KNN classification findings demonstrated that the microfluidic device is highly sensitive to the concentration of non-carboxylated polystyrene beads and can classify concentration levels with 95.0% accuracy. According to a proposed equivalent circuit, the presence of microplastics in droplets can significantly influence the properties of the double-layer capacitance produced at the interface of the droplet and the electrode, making lower frequencies better for discriminating between different concentrations. The prominence of parasitic capacitance at high frequencies makes measurements indeterminate. Finally, it was demonstrated that the droplets' resistive behaviour does not alter as much as the double-layer capacitance behaviour, making medium frequencies less discriminative.

Table of Contents

List of Tables

List of Figures

Lay Summary

In this thesis, a device has been made to detect and measure the concentration of microplastics in water using an electric field. This device is small, fast and reliable. The result of the device was put into further analysis to understand the bahaviour of microplastics in an AC electric field. In comparison to other methods that are commonly used for microplastic detection, this device is cheap, portable, and requires minimal sample preparation.

Preface

The research presented in this thesis is the original work performed by the author. This thesis was supervised by Dr. Mina Hoorfar at the MiNa's lab in the faculty of mechanical engineering at the University of Victoria.

Acknowledgements

I would like to thank CMC Microsystems for providing me with the lock-in amplifier.

I would also like to thank my supervisor, Dr. Mina Hoorfar, our lab manger, Nishat Tasnim, and our postdoctoral fellow Somayeh Fardindoost for their great support.

I am deeply grateful of my parents, my sister, my departed grandfather, and my beloved Rojin, who always supported me.

Dedication

I would like to dedicate this thesis to all the people who fought and lost their lives for freedom.

I would like to dedicate this thesis to Minoo Majidi, Ali Mozaffari, Maziar Soleimanian, Mohsen Mohammadi, Fereydoon Mahmoudi, Reza Lotfi, Farjad Darvishi, Zakaria Khayal, Fouad Ghadimi, Danesh Rahnama, Sadreddin Litani, Milan Haghighi, Amin M'arefat (Maaroufi), Mehdi Asgari, Seyed Mehdi Mousavi, Hadis Najafi, Behnam Layeghpour, Hossein Ali Kia, Mohammad Hossein Sarvari-Rad, Morteza Nowroozi, Javad Heydari, Pedram Azarnoush, Mehrdad Behnam-Asl, Amir Nowruzi, Farzin Lotfi, Sasan Ghorbani, Yasin Jamalzadeh, Ghazaleh Chalavi, Hannaneh Kia, Mahsa Mogouei, Parsa Rezadoust, Saeed Mohammadi, Amir Ali Fooladi, Mehdi (Mohammad) Fallah, Erfan Rezaei, Mohammad Hassan Torkaman, Reza Shahparnia, Mohsen Gheysari, Matin Abdollahpour, Fardin Bakhtiari, Milad Zare, Mohammad Reza Eskandari, Sarina Esmailzadeh, Iman Mohammadi, Nika Shahkarami, Hamzeh Narouei, Abdolrahman Baluchikhah, Mohammad Amin Gamshad-Zehei, Mohammad Reza Adib Tootazehi, Mohammad Brahui, Aminollah Ghaljaei, Emran Shahbakhsh, Yaser Shahbakhsh, Eghbal Shahnavazi, Abu Bakr Ali-Zehei, Jalil Mohammad-Zehei, Hamid Isa-Zehei, Nematollah Kubdani, Hamid Narouei, Samad Shahuzehhei, Mohammad Seddigh Narouei, Lal Mohammad Alizehei, Hamzeh Narouei, Omar Shahnavazi, Abdulghafoor Noor-Barahui, Hamid Narouei, Farzad Shahbakhsh, Mohammad Ghaljei, Mohammad Rigi, Amir Hamzeh Shahnavazi, Lal Mohammad Anshini, Balal Anshini, Salahuddin Gamshad-Zehei, Ebrahim Gorgij, Ahmad Shahbakhsh, Mohammad Eghbal Naebzehei (Shahnavazi), Ahmad Sargolzaei, Mohammad Farough-Rakhsh, Mansour Rakhshani, Abdolmalek Shahbaksh, Ali Akbar Halgheh-Begoosh, Younes Narouei, Jalil Rakhshani, Mohsen Gamshadzehei, Emran Hassanzehei, Yaser Shahouzehei, Amir Hossein Mir Kazehi Riggi,

Mohammad Ali Gamshad-Zehei, Amir Mehdi Farrokhiour, Rafe Narui, Ali Agheli (Narui), Mokhtar Ahmadi, Amir Hossein Basati, Morteza Hassanzani, Zolfaghar Jan Hassanzani, Arman Hassanzani, Mahmoud Hassanzani, Saamer Hashemzehie, Abdollah Mohammadpour, Erfan Kahzaei, Sadis Kashani, Abdolsamad Sabeti Zadeh (Shahu Zahie), Mahuddin Shirouzehi, Javad Pousheh, Suleiman Arab, Abdulghafoor Dahmarde, Esmail Abil, Ahmad Sarani, Amin Goleh Bache, Khodanur Lajai, Mohammad Reza Sarvari, Peyman Manbari, Behzad Rigi, Omid Safarzehie, Najmuddin Tajik, Abdul Wahid Tohidnia, Abdullah Narui, Musa Dovira (Narui), Mohsen Mousavi, Yahya Rahimi (Sarab Shahraki), Omid Sarani, Jaber Shirouzehi, Azizullah Kubdani, Mohammad Rakhshani, Sina Naderi, Armin Sayyadi, Aziz Moradi, Abolfazl Adinezadeh, Abdussalam Qadir Galvan, Arian Moridi, Asra Panahi Jangah, Mustafa Barichi, Abdullah Shahbakhsh, Hamed Baji Zehi, Siavash Mahmoudi, Kamal Feghhi, Erfan Nazarbeigi, Nima Shafagh-Doost, Emad Heydari, Setareh Tajik, Negin Abdolmaleki, Hamid Fouladvand, Mohammad Javad Zahedi, Ali Bani Asadi, Sina Malayeri, Mehrshad Shahidi, Omid Naruie, Adel Kuchakzaie (Barichi), Matlab Saeed Peyro, Esmail Moloudi (semko), Fereshteh Ahmadi, Mohammad Lotfollahi, Keyvan Darvishi, Sarina Saedi, Mohammad Shariati, Kuma Daroftadeh, Shahu Khezri, Zaniar Abubakri, Kobra Sheikh Sagha, Freydoon Faraji, Masoud Ahmadzadeh, Shirin Alizadeh, Mona Naghib, and all other unknown names who have brutally been killed in the passed two months in Iran.

For woman, life, freedom

برای زن، زندگی، آزادی

Chapter 1: Introduction

1.1 Overall Background on Microplastics

Microplastics (MPs) are tiny pieces of plastic waste that have accumulated in the environment. This term refers to a fully heterogeneous mixture of particles ranging in size from a few microns to several millimetres, as well as particles with a variety of morphologies, including entirely spherical and fibre-like particles [1]. Nanoplastics are plastic particles with a diameter of smaller than 100nm. Nanoplastics are likely the most dangerous and least understood type of debris in the aquatic environment [2]. This study will only look at microplastic particles larger than 500nm in size.

Microplastics are generally classified as primary and secondary particles. The difference between primary and secondary microplastics is dependent on whether the particles were designed to be that small from the beginning (primary) or if they were developed as a result of the breakdown of bigger objects (secondary). It is an important difference because it may be used to point out probable sources and pinpoint mitigation strategies to lessen their environmental impact. Primary microplastics include industrial scrubbers used to blast clean surfaces, plastic powders used in moulding, micro-beads used in cosmetic formulation, and plastic nanoparticles utilized in several industrial processes. Secondary microparticles are produced when larger plastic objects are broken apart and weathered. This may occur when using things like paint, tires, and textiles, as well as after they have been discharged into the environment [3].

Many different kinds of polymers can be found as microplastics in the environment. Koelmans et al. assessed polymer types for 32 out of 55 records and the relative frequency of the reported polymer types found in different types of water were taken into account [4]. Table 1-1 shows the

frequencies of studies reporting a particular type of polymer as microplastic particles in 32 out of 55 records reported.

Table 1-1-Frequency of studies reporting microplastic particles of a particular polymer type [4]

Polymer type	*Frequency*
PE	28 (87.5%)
PP	26 (81.25%)
PS	19 (59.4%)
PVC	14 (43.75%)
PET	13 (40.6%)
PA	12 (37.5%)
Acrylic	11 (34.4%)
PEST	10 (31.25%)

Global plastic demand and polymer density may be used to roughly explain the order of the five most prevalent polymers. An order of PE>PP>PVC>PET>PS would result in increased global plastic consumption. PVC and PET have densities of 1.3-1.7 g/cm^3, whereas PE and PP have densities below 1 g/cm^3 and are buoyant, and PS has a density similar to that of water. The lower abundances of PVC and PET in the surface water samples primarily evaluated here may thus be explained by a rather high degree of settling [4].

Size varies the most among microplastic properties. More than six orders of magnitude separate the sizes of microplastic particles, which range from nanometers to millimetres [5]. One of two distinct patterns emerged from the analysis of the data from numerous investigations. They either

demonstrated a decline in particle concentration with increasing particle size, or they discovered an initial rise in concentration with increasing particle size, followed by a decline resembling the first trend. There are two reasons why this initial rise occurred. First, wind mixing, fouling, and aggregation are more likely to affect small microplastics at the water's surface, which would reduce their abundance. Second, because several research projects used visual examination for particles smaller than 0.5 mm, the smallest particles are readily missed in sample analyses, resulting in an analysis bias [6].

The number of microplastic particles present in each sample and kind of water ranges by 10 orders of magnitude. The concentration measurements in the literature do not differentiate between particle size, shape, or material type [4].

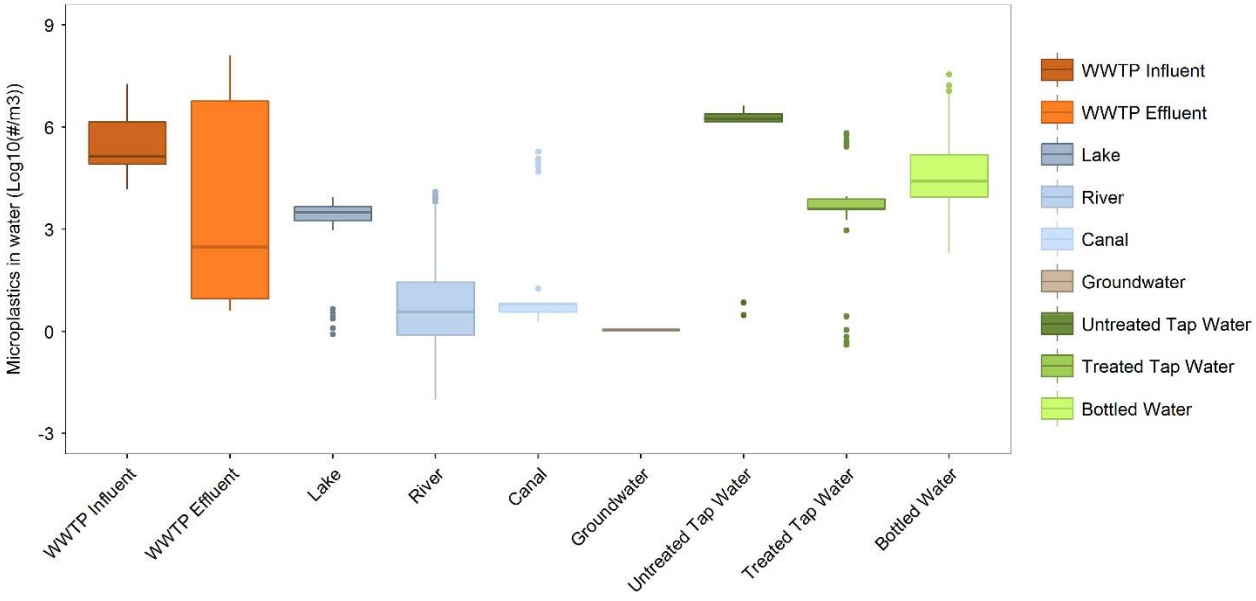

Figure 1-1. The box and whisker diagram depicts the median and variation in microplastic number concentrations in individual samples collected from various water types; with permission [4].

Figure 1-1 illustrates the concentration statistics which show several broad trends. Of all the many forms of water, surface waters have the lowest concentrations, with bottled water being closer to the upper end. Since smaller particles are more prevalent, it is possible that the lower

concentrations seen in surface water, especially when compared to drinking water, are due to the fact that most surface water studies primarily focused on bigger particles [4], [7]. Despite the fact that research on wastewater treatment plants (WWTPs) often did not measure tiny particles, the median and interquartile range of reported values indicate that WWTP influent had the highest concentrations. Because of this, the high concentrations are a reflection of both direct household inputs and inputs from diffuse land-based sources that are transported via wastewater. The difference between the medians of influent and effluent from WWTPs likely reflects the retention of microplastics in WWTPs. Similarly, treated tap water has a greater concentration compared to untreated tap water. Concentrations in bottled water are higher than in tap water, which may be due to a greater intake of airborne particles in the factories, wear from bottle walls or caps after manufacture, or the fact that these studies also included smaller-sized particles [4], [8].

Microplastics' ecotoxicological impacts have primarily been studied in relation to marine creatures up till now. Because human activities are more prevalent in close proximity to the freshwater environment than the marine environment, the potential hazard of pollution there may be greater. Genes, cells, tissues, plants, and animals have all been documented to be affected by microplastics to varying degrees [9].

The existence of microplastics in humans has only been briefly examined in the literature. Human feces included microplastics of sizes 20 to 800 μm [10], the human colon had microplastics of sizes 800 to 1600 μm [11], and human blood contained microplastics of sizes 0.7 to 50 μm [12]. To establish whether exposure to plastic particles poses a risk to the public's health or not, it is necessary to comprehend how these compounds are absorbed by humans and the risks that come with them [12].

1.2 Microplastic Identification Techniques

In this section, we take a look at several potential detection approaches that can be used to identify MPs in different matrices. There will be a discussion of the benefits and drawbacks of each approach, followed by a comparison of those approaches.

1.2.1 Visual Microplastic Identification Techniques

1.2.1.1 Optical Microscopy

Plastic particles may be distinguished from non-plastic by examining their colour, shape, and light transmission. Consequently, optical microscopes may be utilized to produce pictures for examination that reveal the size and form of microplastic particles. Because microplastics smaller than 1 mm are more likely to be ignored or miscounted (non-plastics misidentified as plastics), employing solely microscope identification is appropriate for microplastics larger than 1 mm. Although visual sorting and detection of big microplastics with distinct colours or morphologies are achievable, visual sorting of particles without distinguishable colours or form is difficult. Thus, for recognizing ambiguous plastic-like particles, electron microscopy with enlarged pictures is necessary [13], [14].

Scanning electron microscopy (SEM) combined with energy-dispersive X-ray spectroscopy (SEM-EDS) is widely used for evaluating the morphology of ultra-small materials and determining their elemental composition, allowing for certain capacities of microplastic identification in sample matrices. As most microplastics are non-conductive, SEM-EDS needs extensive sample preparation and analysis time (such as sample drying, sample deposition, and carbon or gold coating), which may introduce artifacts and interfere with the morphological characterization of ultra-small microplastics. Moreover, due to exposure to the high-energy electron beam, thermally

unstable plastic particles may soften or be burnt during the SEM analysis [14] Figure 1-2 shows the SEM images of different polymers of MPs.

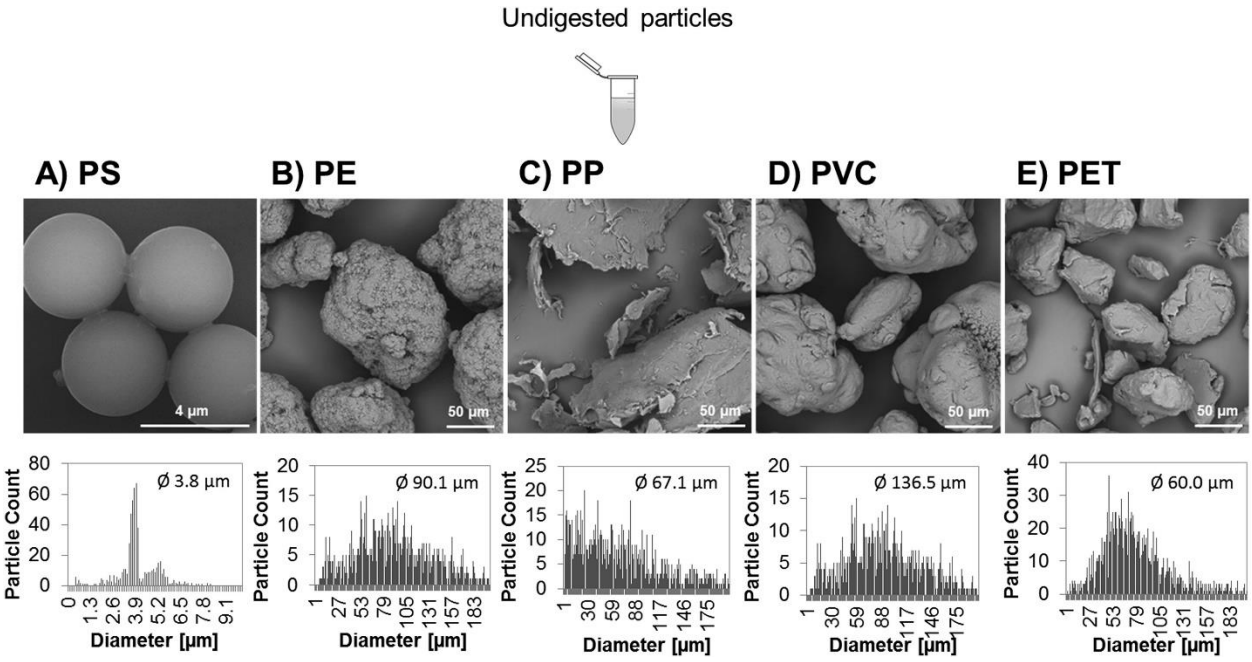

Figure 1-2. Images of (A) polystyrene, (B) polyethylene, (C) polypropylene, (D) polyvinyl chloride, and (E) polyethylene terephthalate microplastics captured by scanning electron microscopy. As established by image analysis, the size distributions of at least 100 particles are shown as histograms with mean diameters; with permission [15]**.**

1.2.1.2 Nile Red

Nile Red (NR) staining is a fluorescent method that shows microplastics in materials, which may be quantified and studied morphologically. NR dye molecules penetrate MPs and bind to polymer surfaces via van der Waals and dipole interactions in polar polymers during staining [16]. The same general NR test procedure has been used by researchers: a sample is collected, chemically pre-treated to eliminate organic debris, dried, stained with NR dissolved in a solvent, and photographed. A filter excludes the excitation wavelength while photographing the dry substance. The image's strong fluorescence identifies MPs [17]. Using the NR approach, the smallest particles that may be detected are between 3 and 6 µm in size [16].

Nile Red staining has been used for the detection of microplastics mainly in water [18]–[20], sediment [21]–[23], soil [24], [25], biota [26], [27], and human-consuming products [28]–[30]. Figure 1-3 is a sample of stained MPs under a fluorescence microscope.

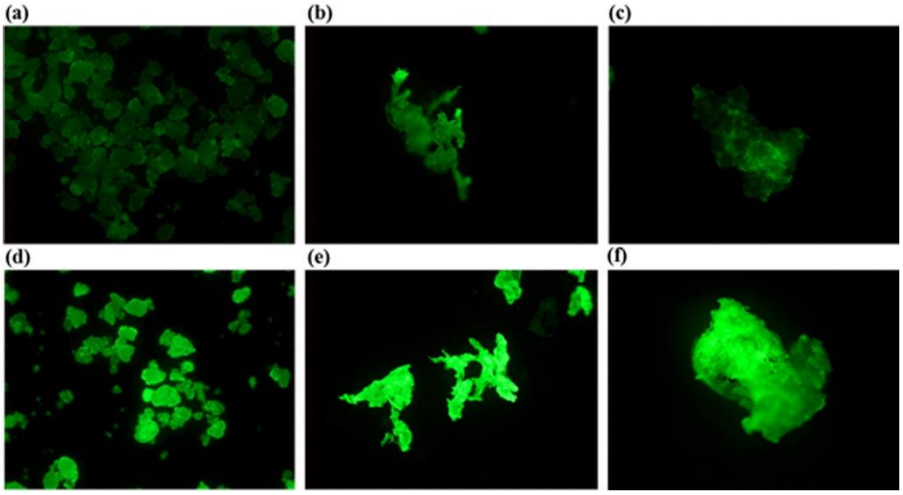

Figure 1-3. (a) low-density polyethylene (LDPE), (b) polypropylene (PP) and (c) expanded polystyrene (EPS) stained with 5 mg/L Nile Red solution and (d) LDPE, (e) PP and (f) EPS with 50 mg/L solution; with permission [31]**.**

1.2.2 Chemical Microplastic Identification Techniques

1.2.2.1 Pyrolysis-Gas Chromatography / Mass Spectrometry (Py-GC/MS)

Pyrolysis is a method that uses heat to break down materials in an inert environment. When applied to plastics, it produces a vapour of particles specific to the kind of the polymer. Then, this vapour is injected into a gas chromatograph where the particles are broken down and sorted based on several physical characteristics. Finally, a mass spectrometer measures the mass of the particles and generates the GC-MS profile of the sample [17]. The type of plastic is identified by contrasting the output of this process with the GC-MS profiles of virgin polymers [32]. In this process, the same sample can be sequentially analyzed under various conditions, such as raising the pyrolysis temperature. Such a sequential process may be a suitable method for obtaining organic plastic

additives (OPAs) at lower temperatures before identifying the polymer pyrolysis products in a single run [33].

Although Py-GC/MS is an excellent approach for identifying MP types, it requires a preliminary screening to separate potential particles. Moreover, quantitative trace analysis of MP on a polymer-specific level is difficult to perform due to the need for highly repeatable pyrolysis conditions. [34]. Very recently, Leslie et al. (2022) utilized Py-GC/MS analysis of human volunteer blood to demonstrate the presence of micro and nano plastics of four highly manufactured polymers [polyethylene (PE), polyethylene terephthalate (PET), polystyrene (PS), and polymethyl methacrylate (PMMA)]. This study found that the average concentration of plastic particles in the blood is 1.6 µg/ml [12].

Py-GC/MS is a reliable method for identifying MP type. However, because this procedure is costly, cumbersome, and time-consuming, it is best suited for laboratory analysis. Additionally, this method is destructive which eliminates the possibility of further analysis of the particles. As the particles must be dried for the pyrolysis process, this method is not suitable for the direct detection of microplastics in aqueous environments. The Py-Gc/MS approach has seen extensive usage in recent years for the purpose of characterizing and identifying MPs in a variety of environmental matrices, including water [35], [36], wastewater [37], soil [38], biota [39], and human-consuming products [40].

1.2.2.2 Fourier Transform Infrared Spectroscopy (FTIR)

Infrared (IR) or Fourier-transform infrared (FTIR) spectroscopy is used to identify microplastics polymeric composition based on their IR spectra. Infrared radiation stimulates molecular vibrations when interacting with a sample. Excitable vibrations are wave-length specific and rely on composition and molecular structure. Depending on the wavelength, IR radiation that excites a

certain vibration is absorbed to a given extent, allowing the determination of distinctive IR spectra. IR spectroscopy is ideal for identifying microplastics because plastic polymers have extremely unique IR spectra and band structures. Non-destructive FTIR spectroscopy has a large polymer database. Comparing acquired spectra to reference spectra identifies polymers. This approach is utilized mostly for analyzing compounds having polar functional groups, such as carbonyl groups [41], [42].

Transmission, reflection, and attenuated total-reflectance (ATR) are FTIR operating modes. ATR-FTIR can accurately assess large particles in under a minute. Micro-FTIR spectroscopy can simultaneously see, map, and gather spectra for tiny particles. Micro-FTIR mapping measures IR spectra at user-defined places on a sample surface. Plastics may be analyzed using transmission or reflectance micro-FTIR. Transmission produces high-quality spectra but needs infrared-transparent materials. Reflectance mode evaluates thick samples. Reflectance mode suffers from refractive error when measuring irregularly-shaped microplastics [43]. Thus, only clear, regular-shaped microplastics may be studied; otherwise, light scattering would distort the signal [41], [42]. Micro-FTIR mapping has been used to identify microplastics; however, the approach is time-consuming and interaction with inorganic particles can harm expensive equipment. Micro-FTIR spectroscopy has a diffraction-limited lateral resolution (e.g. 10 μm at 1000 cm^{-1}), and materials must be dried before IR measurements since water absorbs IR light. Black particles' strong IR absorption makes IR measuring challenging [41], [42].

The FTIR-based methods have been widely used in the characterization and identification of MPs in various environmental matrices such as sediments [43]–[48], water (e.g., seawater [49], [50], fresh water [44], [51]–[54], and bottled water [55]), wastewater treatment plants [56]–[58], biota [59]–[61], humans [62]–[65], salt [66]–[68], and air [69]–[71].

1.2.3 Raman Spectroscopy

Raman spectroscopy is a basic scattering technique that has been used with great effectiveness to detect microplastic particles in various environmental samples. During Raman spectroscopy investigation, a laser with a single wavelength is utilized to excite the molecule. The interaction of laser light with the molecules and atoms of the sample (vibrational, rotational, and other low-frequency interactions) results in changes in the frequency of the backscattered light compared to the frequency of the laser that irradiated the sample. This so-called Raman shift is detectable and results in Raman spectra that are unique to each material. Due to the fact that plastic polymers have distinctive Raman spectra, the approach may be used to identify plastic polymers within minutes by comparing them to reference spectra [41], [42].

As a surface analytical method, Raman spectroscopy permits the analysis of massive, visibly sorted particles. Combining Raman microscopy with Raman spectral imaging enables the generation of spatial chemical pictures based on the Raman spectra of a material. Theoretically, micro-Raman imaging permits the spectrum study of entire membrane filters with a spatial resolution of less than 1 µm. One disadvantage of Raman spectroscopy is that fluorescent materials activated by the laser (such as biological remains in samples) cannot be evaluated because they hinder the creation of interpretable Raman spectra. For a precise determination of the polymer type of microplastic particles using Raman spectroscopy, it is generally advised that samples be purified to eliminate fluorescence prior to observations [41], [42].

The Raman spectroscopy is a complementary vibrational technique for FTIR [72]; thus, similar to FTIR, has been used in environmental matrices such as sediments [73], water [73]–[76], wastewater treatment plants [77]–[79], biota [80]–[84], salt [85], [86], and air [87], and soil [88]–[90].

1.2.4 Physiochemical Microplastic Identification Techniques

1.2.4.1 Hyperspectral Imaging (HIS)

Hyperspectral Imaging (HIS) creates pictures which include spectral information relevant to the scanned components in the sample. Based on how the different chemical species in the sample interact with the different wavelengths of light from the visible to the infrared region, the specific light absorption or scattering shows up as a unique spectrum. The chemical composition and physical structure (e.g., shape, size, and colour) of various materials strongly influence these spectral signatures [14], [91]. Researchers have recently lowered the detection limit of this technique by successfully visualizing and chemically mapping 100nm polystyrene nanoparticles in water suspensions and in vivo [92].

Hypercube is a common term used to describe a hyperspectral image. This is due to the fact that the hyperspectral picture is a three-dimensional (3D) data block comprising a stack of two-dimensional images at different wavelengths. The major characteristic of hyperspectral images is hundreds of continuous and regularly spaced bands. In the hypercube, pictures at neighbouring wavelengths are quite similar, yet images at distant wavelengths may be far less similar and include independent information. In addition, no single wavelength image contains enough information to adequately characterize the item, which is why hyperspectral imaging is important for object analysis [91]. Figure 1-4 depicts a hyperspectral picture of a soil sample covered with PE microplastics and other components.

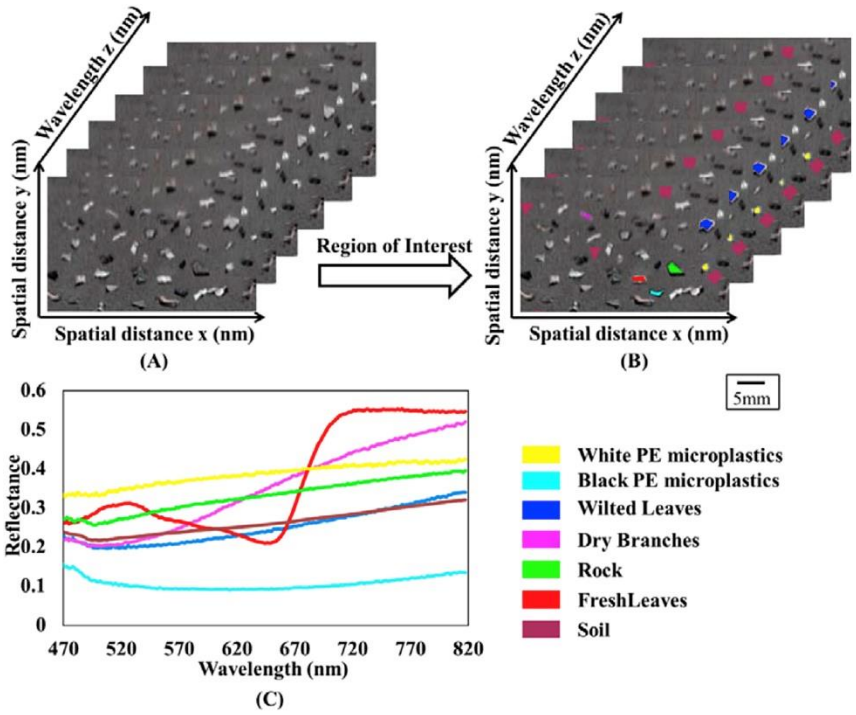

Figure 1-4. (A) Hyperspectral imaging of soil covered with microplastics and other materials; (B) Regions of interest of each type of material; (C) Obtained spectra from regions of interest of each type material; with permission [93]**.**

HSI is a quick, label-free, noninvasive, nondestructive, and reliable imaging system. However, the operating complexity and data processing step of HSI is its most significant drawbacks. HSI requires models or well-known materials to calibrate the pixel information needed to evaluate unknown samples via the model transfer technique. Since the hyperspectral mapping data (pixels per line) are enormous, users must create individualized algorithms to retrieve the desired information. In addition, the comparatively low imaging quality compared to electron microscopes, the low scanning framerates, and the need for academic training prevent the fulfillment of the full potential of HIS [14].

HIS has been used in the detection of microplastics in water [94], [95], wastewater [96] and soil, sand[97], and biota [98]. Recently, this method was shown to have the potential to be used for in situ underwater microplastic detection [99].

1.2.4.2 Dynamic light scattering (DLS)

DLS has extensively studied liquid particle hydrodynamic size and surface charge. A laser beam passes through a liquid solution containing analyte particles that scatter the incoming light at varying angles. The light frequency shift, which depends on particle size, was caused by Brownian motion. The scattered light intensity would fluctuate with light frequency. These variations reveal particle size and shape [14].

DLS has been widely used in biological, physical, and chemical fields to study nanoparticle and microparticle colloidal characteristics. It is non-invasive and operates on a wide range of liquid samples with minimal sample quantities. DLS also characterizes microplastics and nanoplastics [14].

The DLS system scatters light with signal strength proportional to particle radii. Since larger particles scatter more vigorously than smaller ones in a sample, the signals from the bigger particles may dominate the signals of the smaller particles, hiding their presence. Thus, DLS can only assess average size [14].

1.2.5 Electrochemical microplastic identification techniques

1.2.5.1 Resistive pulse sensors

Resistive pulse sensors (RPSs) are based on the Coulter counter principle, which states that transient fluctuations in current are generated by an analyte moving across a tight constriction known as a sensing region. Their simple construction necessitates just two electrodes separated by a constriction and an electrolyte solution. The dimensions of the tight constriction known as the sensing region dictate the sensitivity in these devices since the signal created by the analyte is proportional to the volume of the sensing region it excludes. Tiny sensing regions may detect smaller analytes; however, they need complex fabrication techniques and can cause blockages

when bigger analytes or aggregates are present. Pollard et al. have shown the use of a tunable microfluidic RPS device to detect microplastics with diameters as small as 2 µm. The technology was also tested in real-world applications, such as detecting microplastics in tea bags and distinguishing them from rod and spherical algae [100].

1.2.5.2 Impedance flow cytometry

Microfluidic impedance flow cytometry (MIFC) has been widely employed in single-cell analysis. It employs impedance spectroscopy to assess the electric field screening of individual cells moving

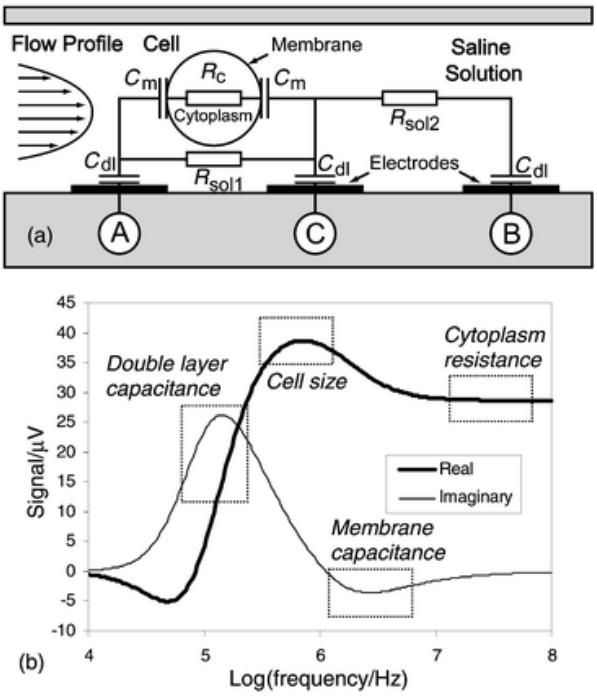

Figure 1-5. (a) A simplified electrical model of the impedance change in the detecting region when a cell is present. (b) A 10 m diameter cell model's simulated complex impedance spectrum [113]**.**

through patterned electrodes in a microchannel via electric current fluctuation under an applied AC voltage. Several factors, including the applied voltage, the system impedance, and the cell characteristics (volume and dielectric constant), all contribute to the temporal change in the current

[101]. The measured impedance varies with frequency. At low frequencies, the cell membrane provides a substantial barrier to the passage of current. The amplitude of the measurement provides information on the volume or size of the cell, which is essentially non-conducting. Low-frequency measurements cannot distinguish between particles with the same volume but differing dielectric characteristics. Measurements at intermediate frequencies will provide details about plasma membrane characteristics. Finally, measurements at high frequencies reveal the dielectric characteristics and the heterogeneous structure inside the cell [102]. Figure 1-5 shows the behaviour of a cell at different frequencies in an MIFC device.

Plastic beads are commonly used for size calibration and testing in MIFC, and they are reliably distinguished from biological particles using a combination of high and low-frequency measurements. Colson et al. have shown the use of impedance spectroscopy for flow-through MP measurement. With a 90% recovery rate and no need for manual sorting or filtering, their technology effectively separated MPs (beads with a diameter of 300 µm to 1000 µm) from biological material [103].

1.3 Comparison of the identification methods

Table 1-2, will examine some of the most significant benefits and drawbacks of the methods that have been covered in this section.

Table 1-2. Comparison of different microplastic detection methods [14], [104]–[107]

Method	*Size limit*	*Pros*	*Cons*
Optical microscope	>1mm	quick and simple; recognizes shape, size, and colour	no proof that the particle is made of plastic; lack of knowledge about the plastic composition;

Method	*Size limit*	*Pros*	*Cons*
FTIR	>20 µm	identifies the polymer composition	Expensive; Analyzing all of the particles retained on the filter is a time-consuming and difficult job; wavelength radiation can be a limiting detection factor; Organic and inorganic contaminants can overlap the polymer bands
Raman	<1 µm	identification of the polymer composition	Very expensive instrumentation; time-consuming; interference with pigments and impurities
SEM/EDS	>5 µm	clear and high-resolution images of particles; Because of the predominant inorganic constituents, it is easier to distinguish between plastic and mineral particles (Si, Ca)	Non-affirmative results in plastic particles; lack of information on the polymer type
Py-GC/MS	-	Concurrent identification and specification of the synthetic polymer and potentially associated additives;	Limited database of virgin polymers; Destructive to the sample Expensive Time-consuming
DLS	>1 nm	Easy sample preparation; high throughput; reproducibility	Bigger particle signals may dominate smaller particle signals, obscuring their presence and producing size bias.
Nile Red	>50 µm	High sensitivity; Inexpensive	Demanding sample preparation requirements; poor elemental sensitivity; Overestimation due to binding to biological contaminations

Method	*Size limit*	*Pros*	*Cons*
HIS	>50 µm	Label-free; non-destructive; reliable	Low signal quality; requires standardized calibration and model transfer methods as an indirect method; Contaminants may cause interferences in chemical identification
RPS	>2 µm	Simple to use; wide concentration detecting range; applicable for most plastics	Limited sizing range; complex sensor fabrication process
IFC	>300 µm	Simple to use; good accuracy; applicable for most plastics; large sensing range	Complex sensor fabrication process; complex data processing; relative low MP recovery rate

The majority of the methodologies that were compared have been put into widespread usage and have been the subject of investigations by various research groups. In microplastic detection, the most frequent procedures include Raman, FTIR, and py-GC/MS; nevertheless, these strategies mostly use expensive and cumbersome instrumentation to perform their analyses. Other procedures could need substantial preparation of the samples as well. The topic of microplastics has seen the least amount of research conducted on electrochemical approaches compared to the other technologies. In the past, impedance flow cytometry has demonstrated that it is quite useful for single-cell analysis. As a result, in order to gain a deeper comprehension of the microplastic identification potential of this approach, we have decided to fabricate and investigate a device that is based on this method.

1.4 Motivation and Objective

This thesis suggests utilizing a microfluidic device to detect microplastics in aqueous samples using impedance spectroscopy. This work focuses on the challenge of determining the size and concentration of microplastics in water droplets, while the count, kind, size, and even form of microplastics are all of the scientific interest. If this objective is achieved, the technology may next be explored using more sophisticated sensors and combined with other measuring strategies to capture additional properties of interest.

1.5 Thesis Outline

The general principles of a microfluidic impedance flow cytometer are presented in Chapter 2. The research experimental procedure is then described. The device's raw output is shown in Chapter 3. The results are post-processed and described in Chapter 4. A review of the accomplishments and anticipated future works is offered in Chapter 5.

Chapter 2: Methodology

2.1 Impedance Flow Cytometry

As a fast-developing technology, MIFC has attracted a great deal of scientific interest. This approach is commonly used for single-cell analysis. Along with their biological sample, several research teams have employed polystyrene beads as a control group. Cheung et al. were able to distinguish between 4, 5, and 6 µm polystyrene beads and red blood cells by measuring impedance at 10 MHz and 602 kHz [102]. Clausen et al. discovered a distinct difference in the measured current response at 200 kHz for 1 µm and 2 µm beads. Furthermore, phase angle measurements at 7 MHz revealed a strong distinction between 1 µm beads and E. Coli. Because of their comparable bulk composition, the 1 µm and 2 µm beads have the same phase angle response [108]. Bernabini et al. were able to distinguish between 1 µm and 2 µm polystyrene microbeads by measuring the impedance magnitude at 503 kHz and the particle speed in the channel [109].

The basics of MIFC as a viable tool for microplastic identification will be described in this section.

2.1.1 Working Principles of an Impedance Flow Cytometer

Multiple alternating current (AC) stimulation impulses are delivered concurrently to the excitation electrodes. A differential amplifier measures the current flowing through the system from the detection and reference volumes. After being processed by a lock-in amplifier, the resulting signal is split into its in-phase (Real) and out-of-phase (Imaginary) components as per frequency. Particles in suspension would move across the electric field created inside the microchannel, between the excitation electrodes and the measuring electrodes. The presence of the particle in the sensing zone would cause the measured currents to vary. This variation is determined by the particle's inherent characteristics at the excitation frequency [101], [110].

In a microfluidic impedance flow cytometer, the analysis volume between the electrodes determines how sensitive the device may be. While a low volume results in great sensitivity, it also increases the likelihood that the device may become clogged and rises difficulties in the fabrication process [101], [109]. When a particle fills a substantial percentage of the space between the measuring electrodes, the observed signal can be enhanced. Therefore, channels with dimensions comparable to the particle's diameter are used for impedance measurement. Furthermore, SNR improves as excitation voltage rises. Increasing the voltage, on the other hand, may cause electrochemical reactions at the electrodes, resulting in corrosion and/or bubble formation, especially at low frequencies in high-conductivity mediums [101], [111].

Characterizing particles requires probing them throughout a wide frequency range because, depending on their dielectric characteristics, various features will react at different frequencies. However, Faradaic reactions at metal electrodes could happen at low frequencies (0.1 MHz), leading to corrosion. In addition, the DC and low-frequency components of the signal are dominated by a double-layer capacitance that develops over metal-based electrodes, lowering the signal-to-noise ratio. The lowest stimulation frequency is often a compromise between the need for particle size sensitivity and the need to improve SNR. However, at high frequencies, the device's sensitivity will be altered by the existence of stray capacitances in parallel with the measurement sample, which will shunt the channel impedance [101].

To control how much and at what frequencies a field line travels through the particle vs the medium, the dielectric characteristics of the suspension may be adjusted. 1 M PBS solutions are commonly used, with the formulation optimized for best conductivity. In the typical working range (0.5-50 MHz), reducing the suspension medium to 0.5 M or lower increases field penetration to more interior areas of the sample, highlighting variations between subpopulations; however, this

comes at the expense of an increase in measurement noise owing to voltage drops from the system impedance [101].

2.1.2 Electrode Configuration

2.1.2.1 Coplanar Electrodes

Coplanar electrode configuration is used for absolute or differential measurements, and it comprises patterned electrodes placed on one side of a microchannel. In an absolute measuring system, two electrodes are typically positioned at the channel's bottom or top. A sensing region is created when an alternating current voltage is supplied across the electrodes. Particles passing through this region alter the electric field between two electrodes, leading to a change in current from which dielectric property information may be extracted. A differential measuring system has three electrodes, with an AC voltage delivered to the central electrode and electric currents with opposing phases detected at the lateral electrodes. It is possible to detect the electric current fluctuation caused by a particle's passage through the first half of the sensing zone, while the second half gauges the electric current flowing through the medium itself. The differential fluctuation in impedance is shown as a pair of peaks due to the intrinsic reversal of the measuring and reference electrodes (Figure 2-1). In most cases, trans-impedance amplifiers may be used to convert the electric current recorded by two lateral electrodes into voltage signals. An enhancement in sensing sensitivity and correction for unequal drift in electrode characteristics are both possible with this differential impedance sensing approach. As a result, it is the most often used structure for single-cell impedance sensing [112].

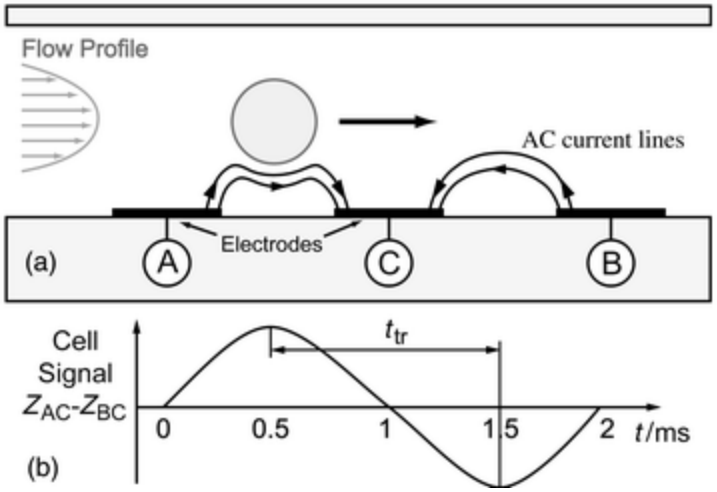

Figure 2-1. (a) A schematic side view of the microchannel with a particle travelling through three electrodes (A, B and C). The differential impedance signal (Z_{AC}-Z_{BC}) is monitored. (b) Impedance signal. The particle's speed may be determined after the distance between the two measurement locations and the time t_{tr} between the signal spikes are known. The reference and measurement electrodes in this type of sequential differential sensor are naturally switched, displaying uneven drift of electrode characteristics; with permission [113]**.**

The impedance signal varies with the particle's height in the sensing zone because of the nonhomogeneous electric field generated by the coplanar electrodes. Thus, these impedance sensing designs are most suited for large bioparticles (with dimensions of 100 µm-1 mm). Small bioparticles (20 µm) might be difficult to detect with MIFC devices due to the positional dependency of the impedance sensing signal. As a result, several particle-focusing methods have been included in the three-electrode impedance cytometry in order to get over this drawback [114]–[116]. With this type of impedance sensor, the differential signal has a bipolar Gaussian shape. Information about particle velocity and height, which may be used to rectify the observed electrical diameter, can be inferred from the relative prominence of the peaks relative to the saddle between them [112].

MIFC devices are often put to use in situations where very concentrated suspensions of particles must be managed. However, errors in detecting the characteristics of these particles may occur if two or more particles pass through the sensing zone almost simultaneously [112]. A Bayesian approach has been proposed using two successive electrical sensing zones and maximum a posteriori probability estimation to resolve the coincidence problem in MIFC [117].

The three-electrode arrangement is one of the most popular systems because it is simple to fabricate and provides a reasonably good signal-to-noise ratio (SNR) for particle sensing; nevertheless, the problem of electric field nonuniformity has not been well addressed. It has been suggested that reducing the channel's or sensing zone's cross-sectional area may improve performance. However, this approach runs the risk of causing clogging and thereby lowering the sensing throughput. It is also possible to improve sensor sensitivity by employing signal correction algorithms based on electrical metrics of particle location. Unfortunately, this typically necessitates additional, more involved, and time-consuming data processing stages [112].

2.1.2.2 Facing Electrodes

The facing electrode design typically consists of parallel electrode arrays, with electrodes positioned at the channel's top and bottom (Figure 2-2). Both absolute and differential measurements may be taken with this setup. The electric field distribution between parallel-facing electrodes is more homogenous (but not totally uniform), making it better suited for very sensitive impedance detection than the coplanar. Typically, an alternating current (AC) voltage is given to the top electrodes (excitation electrodes), while the bottom electrodes (sensing electrodes) are utilized to receive response signals. Similar to the coplanar design described above, the mechanism behind particle sensing involves recording the change in current caused by the passage of the particle between the facing electrodes and then analyzing the resulting data. It has been shown that

the particle's position in the channel still impacts the impedance signals due to the non-uniformity of the electric field, as the strength of the electric field near the stimulating electrode is greater than that near the sensing electrode. To get around this problem, scientists directed particles to the channel's center before they entered the sensing region. Furthermore, the non-homogeneity of the electric field and diagonal current flow between the diagonal electrodes cause the impedance signal to vary with respect to the particle locations in two or more pairs of parallel-facing electrodes. Researchers have shown that lowering the size of the channel or increasing the distance between electrodes in the same plane can reduce the positional dependency of impedance, but at the sacrifice of sensitivity or throughput. To address these issues, a signal-processing compensation approach was used in the facing electrode design. This method of compensating for the positional

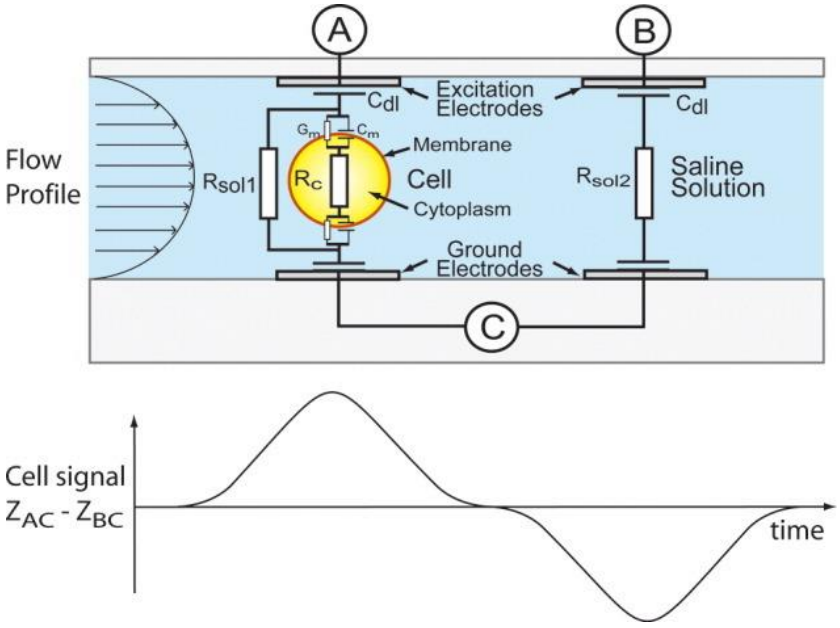

Figure 2-2. Side view of a microfluidic channel displaying a sample cell travelling between the measurement and reference electrodes. As the cell passes through the detecting area of the microchannel, the expected shape of a sample output from the lock-in amplifier; with permission [102]**.**

dependency of the signal in signal processing is effective, but it imposes a heavy computing burden on the post-processing of huge amounts of data [112].

Despite the fact that the facing electrode layout generates a more uniform electric field distribution and is more sensitive since the electric field is restricted to a smaller detection volume, this design calls for a more intricate fabrication process due to alignment requirements and the difficulty of bonding the SU8 to glass. Therefore, it is crucial to find a less complicated fabrication process that may be used for a wider range of applications [101], [112].

2.1.2.3 Liquid Electrodes

In a liquid electrode configuration, dead-end chambers are positioned on each side of the main channel, with electrodes at the bottom of each (Figure 2-3). In most cases, this setup can provide a uniform electric field over a wide region and at the main channel's full height. This sensor is significantly easier to manufacture than those with a facing electrode layout. However, the sensitivity is decreased due to the longer detection length and hence greater detection volume [101], [112].

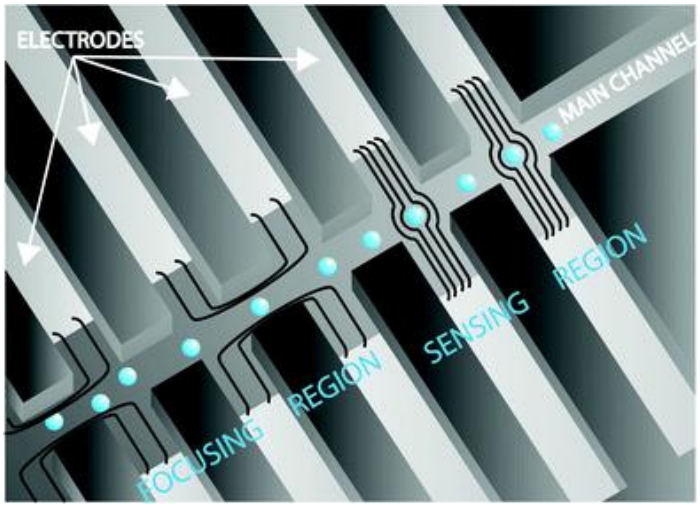

Figure 2-3. Schematic of the chip that uses the same liquid electrode design for both impedance measurements and dielectrophoretic focusing; with permission [118]**.**

2.2 Experimental Setup and Procedure

This chapter details the micro-fabrication processes that went into making the MIFC device. There is also a detailed explanation of how the experiments were conducted, as well as the materials and setup used.

2.2.1 Device Fabrication

In this section, the fabrication of the electrodes and the microchannels is described. The coplanar electrodes were designed to have a width of 60 µm and 60 µm gap. The microchannels were designed to have 60 µm width and 40 µm height.

2.2.1.1 Electrode Fabrication

For its high electrical conductivity and reliability, gold was used as the conducting layer. Gold and glass, on the other hand, do not adhere to one another very well. In order to promote adhesion, chromium is often placed as a coating on the glass. On 100mm Borofloat33 Glass Wafers (University Wafer, Inc.), a 10-nm layer of chromium and a 100-nm layer of gold were sputtered by a magnetron sputtering system (MANTIS Deposition LTD.) (Figure 2-4a).

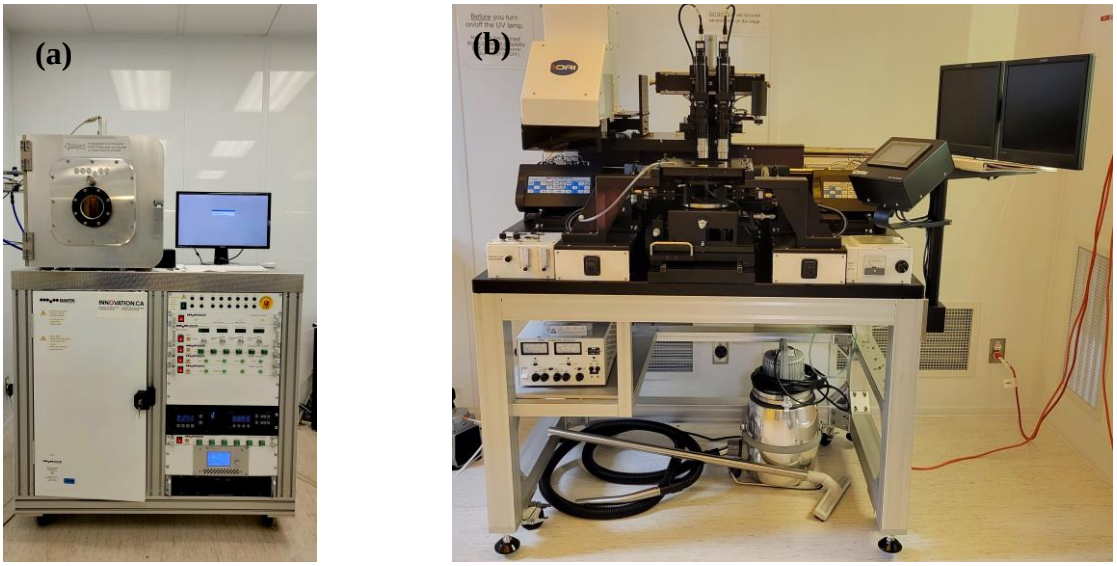

Figure 2-4. (a) The sputtering machine, (b) the mask aligner.

Standard photolithography was used to create the electrode patterns. First, a glass wafer with gold sputtered on top was coated with a layer of positive photoresist, S1813 (The Dow Chemical Company), using a spin coater (Laurell Technologies). The substrate was then placed in a mask

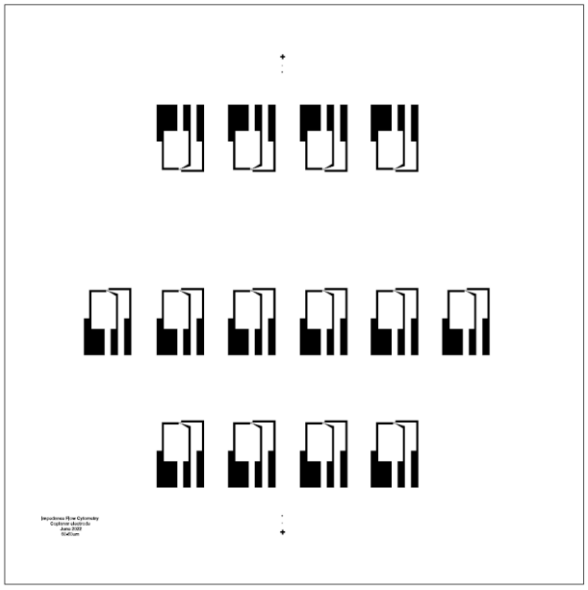

Figure 2-5. The photomask that was used in for electrode fabrication

aligner (OAI model 804) (Figure 2-4b), where it came into direct contact with a photolithography mask and was exposed to UV light for 12 seconds (150 mJ/cm^2). The mask was made in AutoCAD 2022, and CAD/Art Services, Inc. printed it (Figure 2-5).

Afterwards, the chip was submerged in a photoresist developer (MF-319 developer, Kayaku Advanced Materials, Inc.) to remove any remaining unexposed photoresists. Then, the excess gold and chromium were etched away using gold and chromium etchants (Sigma-Aldrich). Next, a photoresist remover (MICROPOSIT® REMOVER1165, Kayaku Advanced Materials, Inc.) was used to get rid of any leftover traces of the photoresist. The chip was then cleaned by rinsing it with DI water and drying it with compressed air.

2.2.1.2 Channel Mould Fabrication

To create the microchannels made of PDMS, SU8 structures were fabricated on silicon wafers in a cleanroom to serve as moulds. To begin, a 3-inch silicon wafer (WaferPro) was spin-coated with SU-8 3025 (Kayaku Advanced Materials, Inc.). This was followed by employing a two-step spin coating process. After spinning the substrate at 500 rpm for 10 seconds at an acceleration of 100 revolutions per second, the wafer was completely covered with SU-8. The SU-8 was spun at 1800 rpm for 45 seconds at an acceleration of 300 rpm/second to accomplish a height of 40 µm. The wafer was then soft baked for 15 minutes at 95 degrees Celsius. The next step was to expose the wafer to UV light beneath a photolithography mask (CAD/Art Services) for 16 seconds (212 mJ/cm^2), which allowed only the UV light necessary to crosslink the SU8 to the desired pattern on the chip to pass through the mask's transparent area. Figure 2-6 shows the photomask which was used to fabricate the microchannels.

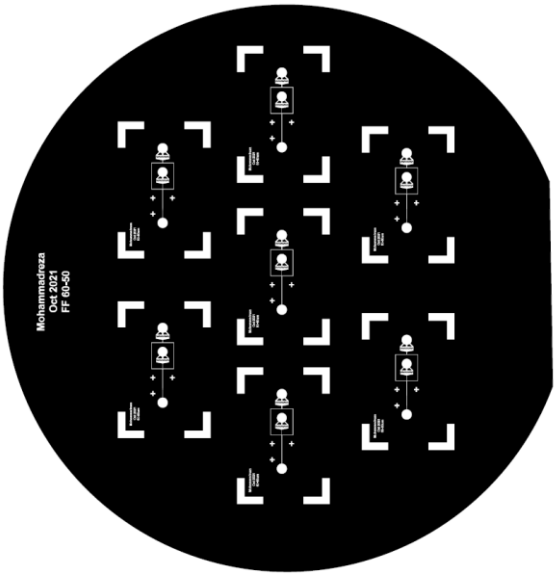

Figure 2-6. The photomask used for channel fabrication.

As soon as the exposure is complete, a post-exposure bake should be performed. The wafer is baked for 1 minute at 65 ° C and 5 minutes at 95 ° C. The wafer was then placed into a container

of SU8 developer (Kayaku Advanced Materials, Inc.) and left there for 8 minutes while the solution was gently agitated. After an isopropanol wash, the wafer was resubmerged in fresh SU-8 developer for a few seconds. After a final isopropanol rinse, the wafer was hard-baked at 150 °C for 30 minutes to anneal any surface fractures. The final product of this process is shown in Figure 2-7.

Figure 2-7. The final microchannel mould

2.2.1.3 Channel Fabrication

After the PDMS and its curing agent (Dow Corning's SYLGARDTM 184 Silicone Elastomer) were thoroughly combined with a weight ratio of 10 to 1, the mixture was put into the fabricated mould. The solution was degassed in a desiccator for about half an hour before the PDMS was cured on a hotplate at 75 degrees Celsius for about three hours. After peeling off the PDMS, inlet and outlet holes were punched (using a Miltex® Biopsy Punch with Plunger, ID 1 mm) and the

surface was cleaned using a 3M tape. Figure 2-8 shows the PDMS microchannels before punching the inlets and outlets.

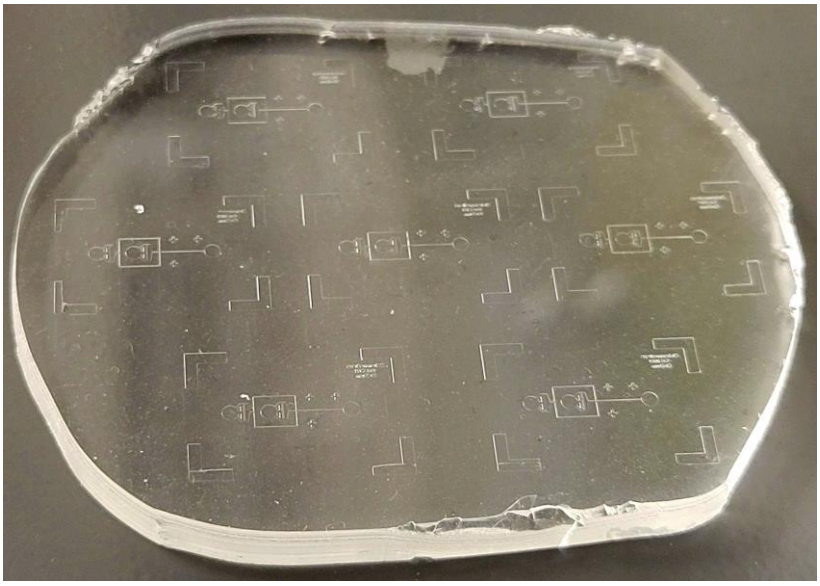

Figure 2-8. A block PDMS pilled off the mould.

2.2.1.4 Electrode and Microchannel Bonding

Initially, the electrodes were cleaned to eliminate any residue from the gold pattern. For this purpose, they were first shaken for 15 minutes in acetone. The samples were then rinsed with new acetone and agitated for three minutes in isopropyl alcohol. After that, a plasma treatment (PE-50, PLASMA ETCH) was performed for 15 seconds at 67.5 Watts power, and 30 cm3/min oxygen flow rate on the PDMS channel and electrode slide (Figure 2-9a). A customized, benchtop aligner was used to attach the oxygen plasma-treated channel to the substrate (Figure 2-9b).

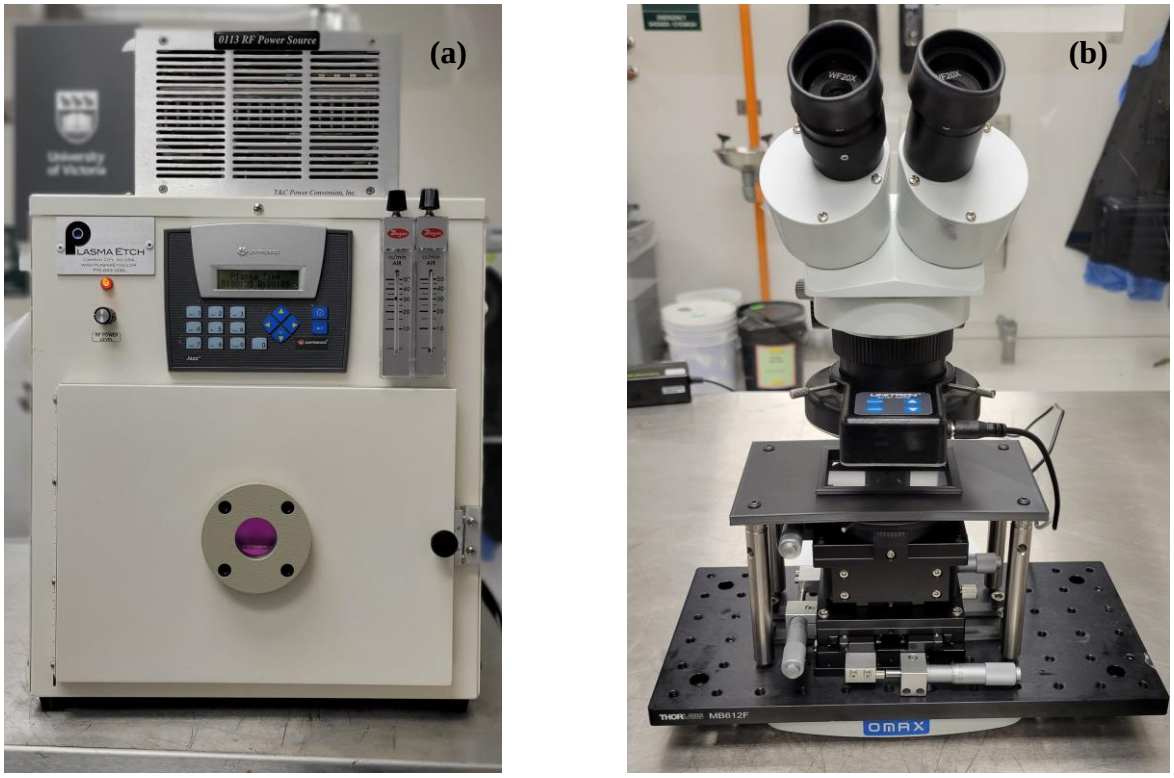

Figure 2-9. (a) Using plasma to bond PDMS and glass. (b) The benchtop aligner

Finally, the chip was left on a hotplate set to 80 ℃ overnight, to achieve complete bonding and hydrophobic channel walls. Figure 2-10 shows the channel after alignment and bonding.

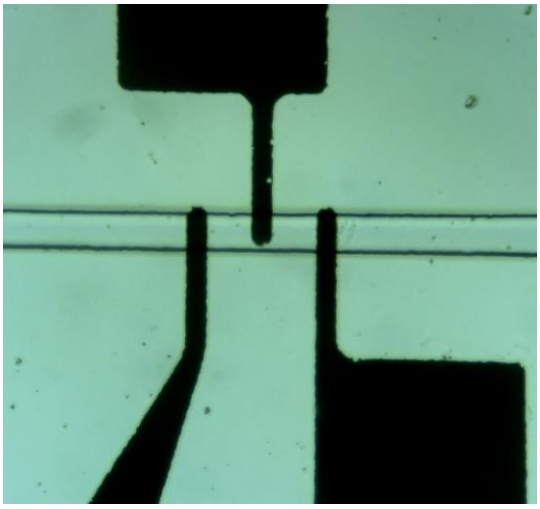

Figure 2-10. The coplanar electrodes at the bottom of the microchannel

2.2.2 Measurement Setup

An HF2LI-MF lock-in amplifier (Zurich Instruments, Zurich, Switzerland) and an HF2TA trans-impedance amplifier (Zurich Instruments) were used to record the impedance data (Zurich Instruments). Multiple signal frequencies can be captured at once using the lock-in amplifier. Different frequencies of 4.4 MHz at 8V, 11 MHz at 1.5 V, and 22.5 MHz at 0.5 V were employed here. The first frequency was chosen by incrementally increasing the frequency to get all components of the signal with a relatively good signal-to-noise ratio. Voltages were chosen so as to prevent amplifier saturation. Differential input impedance, alternating current coupling, and a sampling rate of 14.39 kSa/s via a 4th-order low-pass filter with a time constant of 3.028 ms were the parameters used to set a lock on the amplifier. The lock-in amplifier was linked to the microfluidic chip through a customized cable and printed circuit board mounted on an acrylic glass chip holder Figure 2-11a. Figure 2-11b illustrates the whole setup that was used in this research.

2.2.3 Data Acquisition and Analysis

LabOne® was used to operate the lock-in amplifier. Initially, the real and imaginary components of the signal, as well as its amplitude and phase, were recorded in LabOne. The data was then transferred to Matlab for additional processing. Peaks were extracted from each component in Matlab, and the prominence of each peak was saved as the needed information.

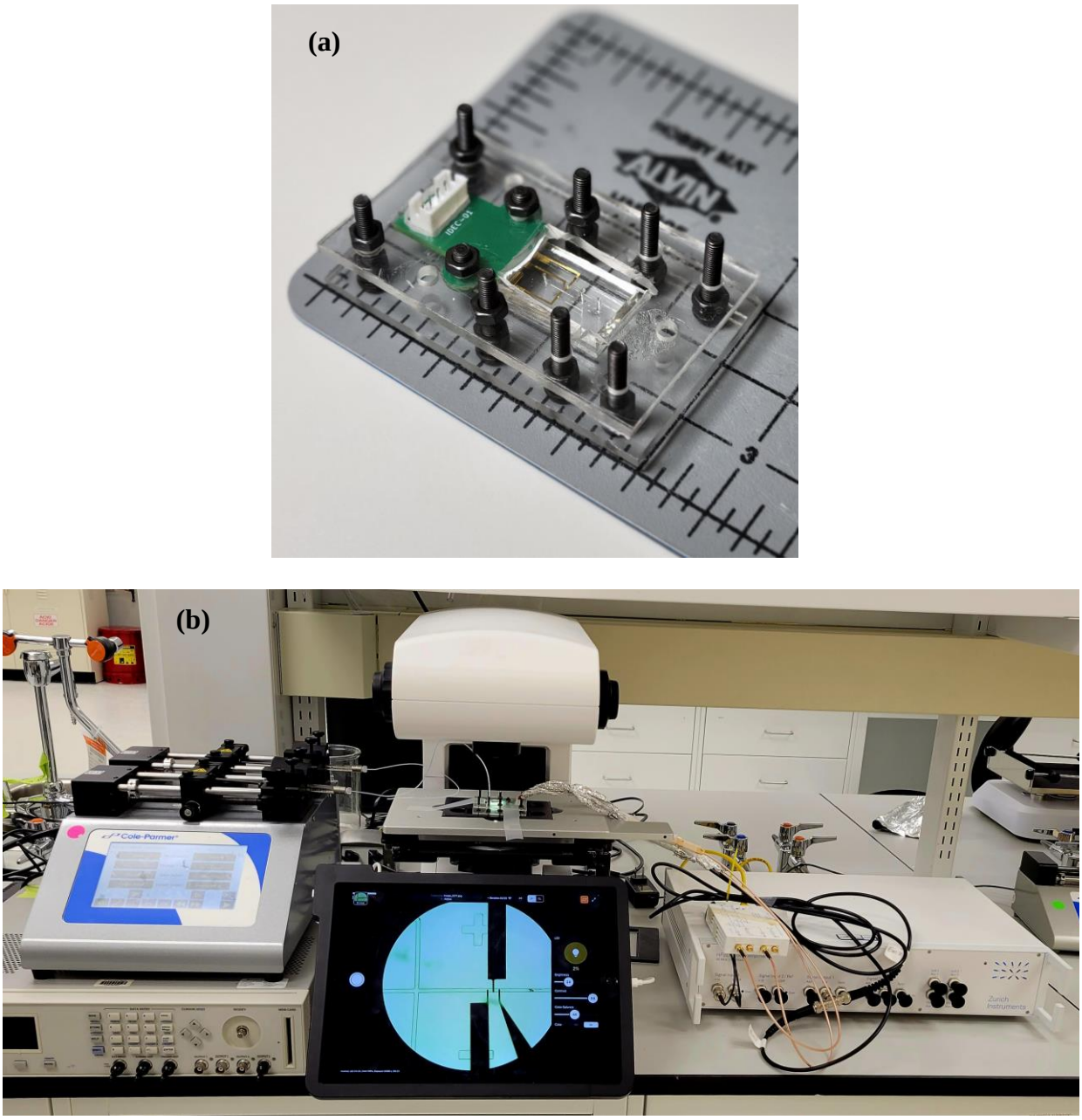

Figure 2-11. (a) The final assembly of the chip. (b) The complete setup to perform the experiments

2.2.4 Sample Preparation

Because this experiment was conducted using a droplet-based microfluidic system, mineral oil was used as the continuous phase and an aqueous-based mixture as the dispersed phase. As a surfactant for the continuous phase, span 80 was added to mineral oil. The solution was then thoroughly

stirred on a magnetic stirrer at 50 °C and 400 rpm for 3 hours. The dispersed phase was made up of four different sizes of polystyrene microbeads dispersed in DI water as well as pure DI water. Microparticles with diameters of 500 nm (Phosphorex, Inc), 1 µm (Polysciences, Inc), 3 µm (Polysciences, Inc), and 6 µm (Phosphorex, Inc), were diluted from their original solid content percentage to final concentrations of 0.05%, 0.10%, and 0.20% solid particle percentage (g/ml).

2.2.5 Experimental Procedure

A full factorial design of the experiment was used, with two variables (solid particle concentration and particle size). There were three levels of solid particle concentration (0.05%, 0.10%, and 0.20%) and four levels of particle size (500nm, 1 µm, 3µm, 6µm). Each level combination was repeated twice. The experiment design is illustrated in Table 2-1.

Table 2-1-The full factorial design of the experiment

EXPERIMENT	**EXP 01**	**EXP 02**	**EXP 03**	**EXP 04**	**EXP 05**	**EXP 06**	**EXP 07**	**EXP 08**
SIZE	3 µm	0.5 µm	1 µm	3 µm	3 µm	0.5 µm	1 µm	6 µm
CONCENTRATION	0.10%	0.05%	0.10%	0.20%	0.20%	0.10%	0.20%	0.20%
EXPERIMENT	**EXP 09**	**EXP 10**	**EXP 11**	**EXP 12**	**EXP 13**	**EXP 14**	**EXP 15**	**EXP 16**
SIZE	0.5 µm	6 µm	1 µm	6 µm	0.5 µm	3 µm	6 µm	3 µm
CONCENTRATION	0.20%	0.10%	0.05%	0.20%	0.20%	0.10%	0.10%	0.05%
EXPERIMENT	**EXP 17**	**EXP 18**	**EXP 19**	**EXP 20**	**EXP 21**	**EXP 22**	**EXP 23**	**EXP 24**
SIZE	6 µm	1 µm	1 µm	0.5 µm	1 µm	6 µm	0.5 µm	3 µm
CONCENTRATION	0.05%	0.05%	0.20%	0.05%	0.10%	0.05%	0.10%	0.05%

In addition to the tests listed in Table 2-1, two more experiments with pure DI Water were performed at the beginning and end of the series of experiments.

Using a dual syringe pump, the dispersed and continuous phases were pumped into the microchannel from 250 µl and 1 ml syringes, accordingly. To obtain constant slugs, the flow rates of the dispersed and continuous phases were kept constant at 150 µl/min and 500 µl/min, respectively. The output was linked to a tube, which was used to collect and dispose of the samples

after use. 256000 data points (about 9 seconds) were gathered for each experiment. Following each experiment, the microchannel was flushed with continuous phase and then DI water. To ensure the consistency of the channels, the tests were carefully observed under a microscope.

Chapter 3: Results

Each droplet produces two peaks in the signal read by the lock-in amplifier. The output signal is at its baseline before a droplet enters the electric field (state 1 in Figure 3-1). The first peak appears as soon as the droplet enters the detecting zone. The signal reaches its maximum when the droplet completely covers the initial gap between the excitation and sensing electrodes (state 2 in Figure 3-1). When a droplet enters the second gap between the excitation and sensing electrodes, a signal with the opposite sign of the first peak is produced (state 3 in Figure 3-1). As a result, the second peak will be about the same height as the first, but in the opposite direction. Figure 3-1b depicts a piece of a raw signal from one of the experiments. The prominence of the positive peak was extracted for each frequency component. Figure 3-1b depicts a selection of recorded peaks used for further analysis.

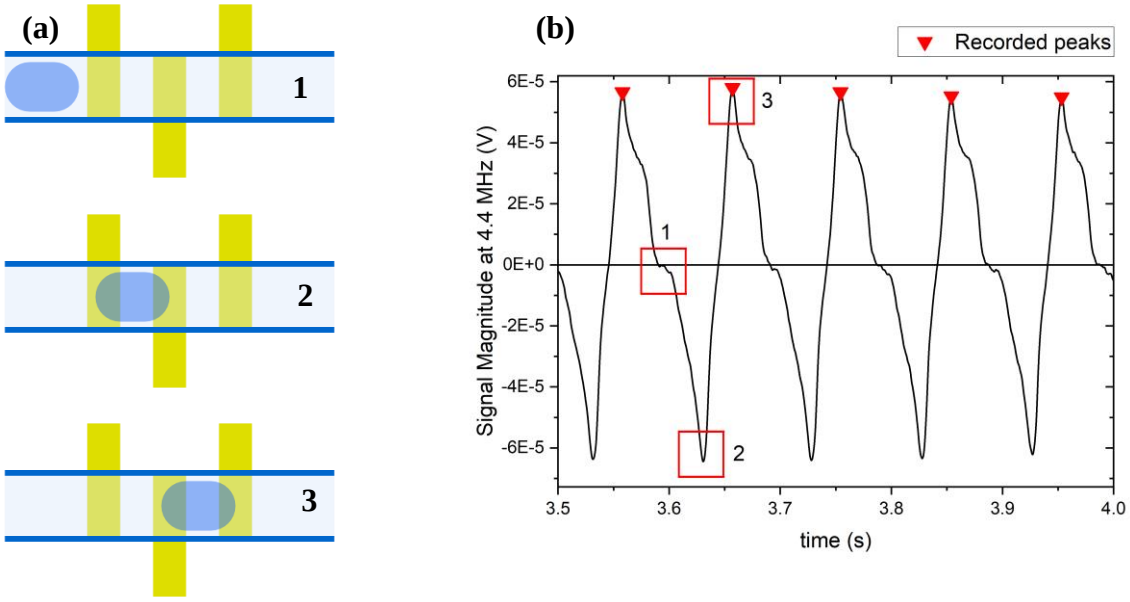

Figure 3-1. (a) The position of the droplet regarding the electrodes. (b) The corresponding signal that is observed on the computer

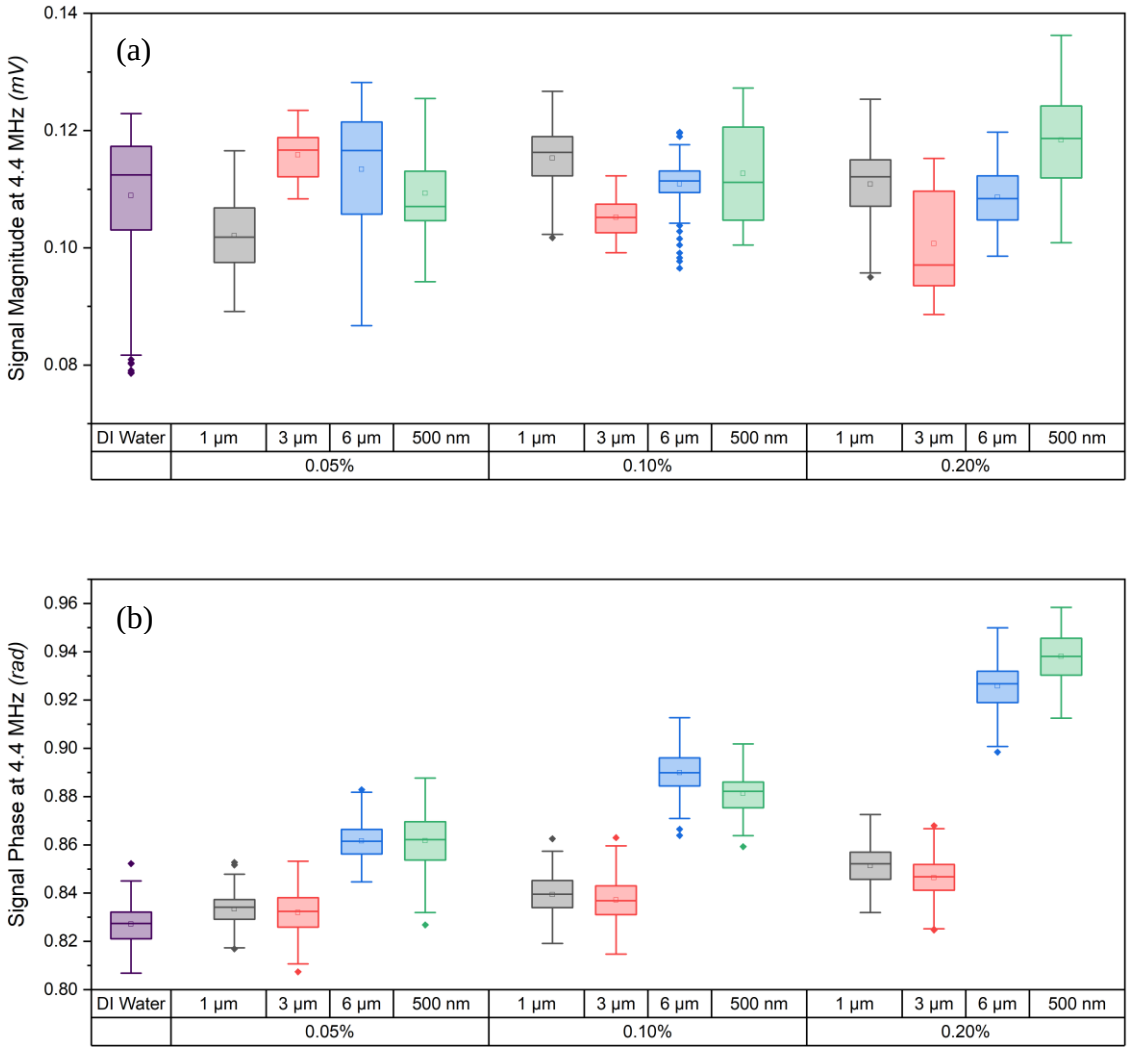

Figure 3-2. The box and whisker plot of the measurements at 4.4 MHz. (a) The signal magnitude. (b) The signal phase

In total, 13164 peaks were identified for the signal's magnitude, phase, real component, and imaginary component. Following a visual examination of the scatter plots, the polar representation of the data was chosen to better depict the data. First, all of the data was subjected to a normality test. A normal distribution was found solely for the phase measurement. This could be because there was no active control or measurement of the slug size, which could have changed the signal magnitude. Nonetheless, the ratio-based character of the phase ($\tan^{-1}(Y/X)$) has likely nullified the

influence of the size and normalized the data. The box plots of all the data were then shown at each frequency to visually compare the data statistics.

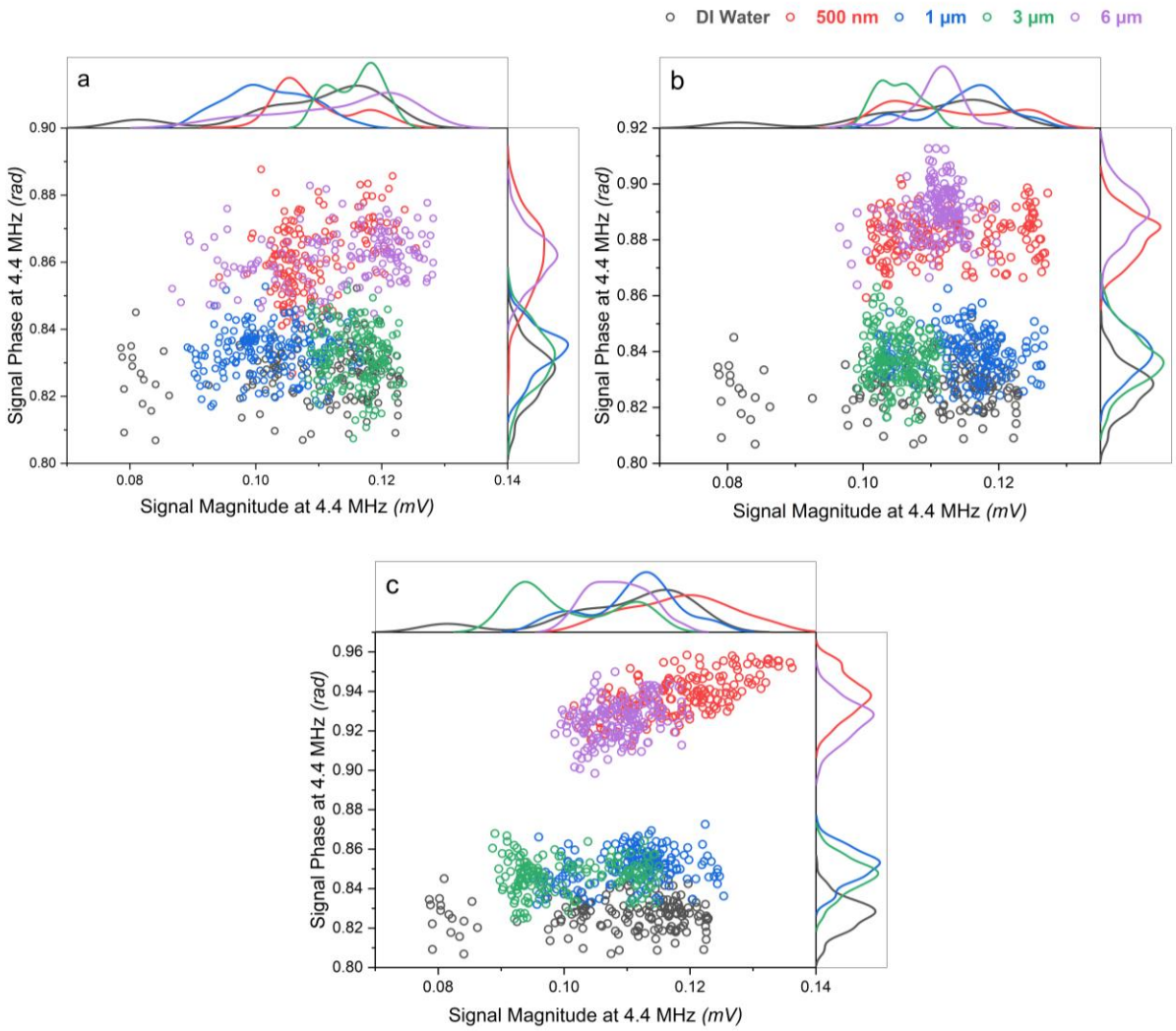

Figure 3-3. The scatter plot with the marginal histogram of all the peaks detected at 4.4 MHz for different concentrations of a) 0.05%, b) 0.10%, and c) 0.20% solid particle.

3.1 4.4 MHz measurements

The first set of box plots of the measurement at the lowest detected frequency, 4.4 MHz, is shown in Figure 3-2. Figure 3-2(a) shows that neither the concentration nor the particle size had any effect on the signal magnitude. Furthermore, the data does not follow a regular pattern. As a result, the

change in signal magnitude at the lowest recorded frequency provides no helpful information.

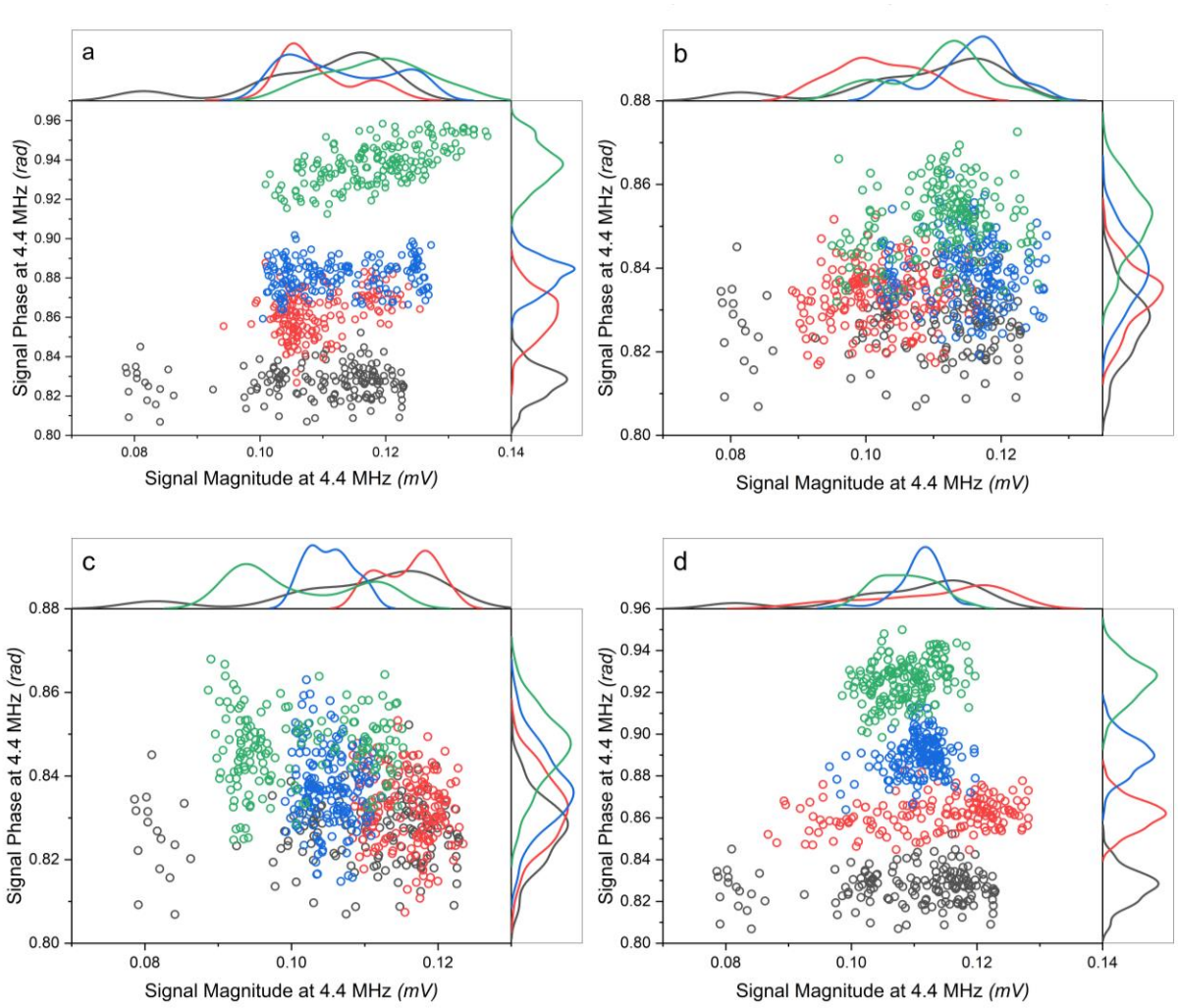

Figure 3-4. The scatter plot with the marginal histogram of all the peaks detected at 4.4 MHz for different particle sizes of a) 500 nm, b) 1 µm, c) 3 µm, and d) 6 µm.

Figure 3-2(b), on the other hand, clearly displays the effect of particle concentration on the signal phase at 4.4 MHz. The addition of particles to DI water increases the phase of the signal, resulting in a more capacitive medium for the electric field. Furthermore, it is demonstrated that 1 µm and 3 µm particles behave quite similarly, as do the other two particles. This resemblance will be

examined more in the future. ANOVA was used on this set to demonstrate the differences statistically as well.

Figure 3-3 displays scatter plots for all data points for various droplet compositions at each concentration. The distribution's normality in the phase direction is clearly demonstrated. 500 nm and 6 µm particles, as well as 1 µm and 3 µm particles, are clustered together in all concentrations. The x-direction measurement distribution (signal magnitude) is generally bimodal.

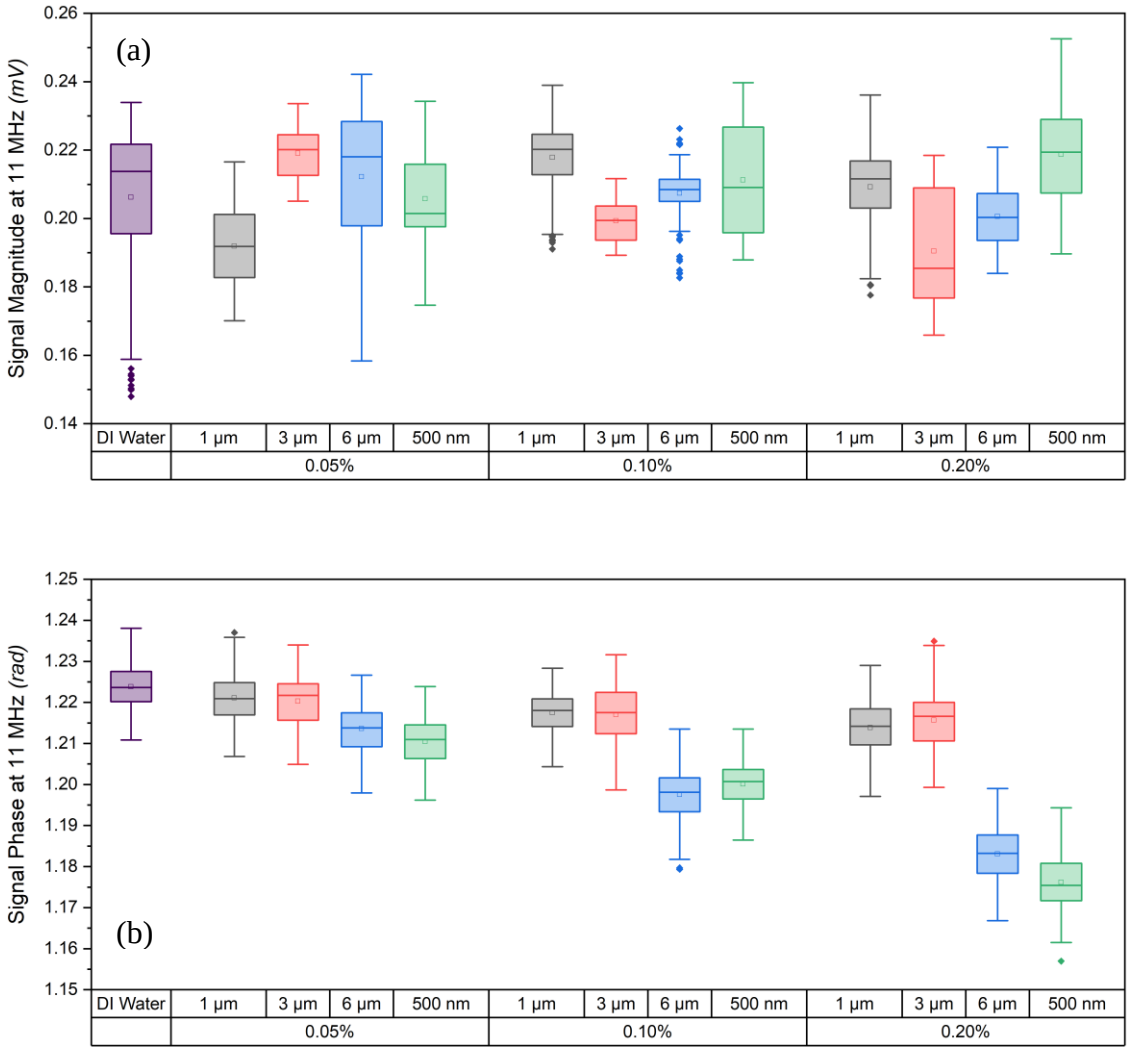

Figure 3-5. The box and whisker plot of the measurements at 11 MHz. (a) The signal magnitude. (b) The signal phase

Figure 3-4 represents the distribution of observations at 4.4 MHz for each particle size at various concentrations. The addition of microparticles would undoubtedly raise the signal phase of all particles. For 1 and 3 µm microparticles, the shift is subtle.

3.2 11 MHz Measurements

The polar measurement of the signal at 11 MHz is shown in Figure 3-5. Similarly to section 3.1, the magnitude of the signal provides little information on the influence of microplastic presence in the droplets. However, phase measurements generally decrease as microplastic concentration

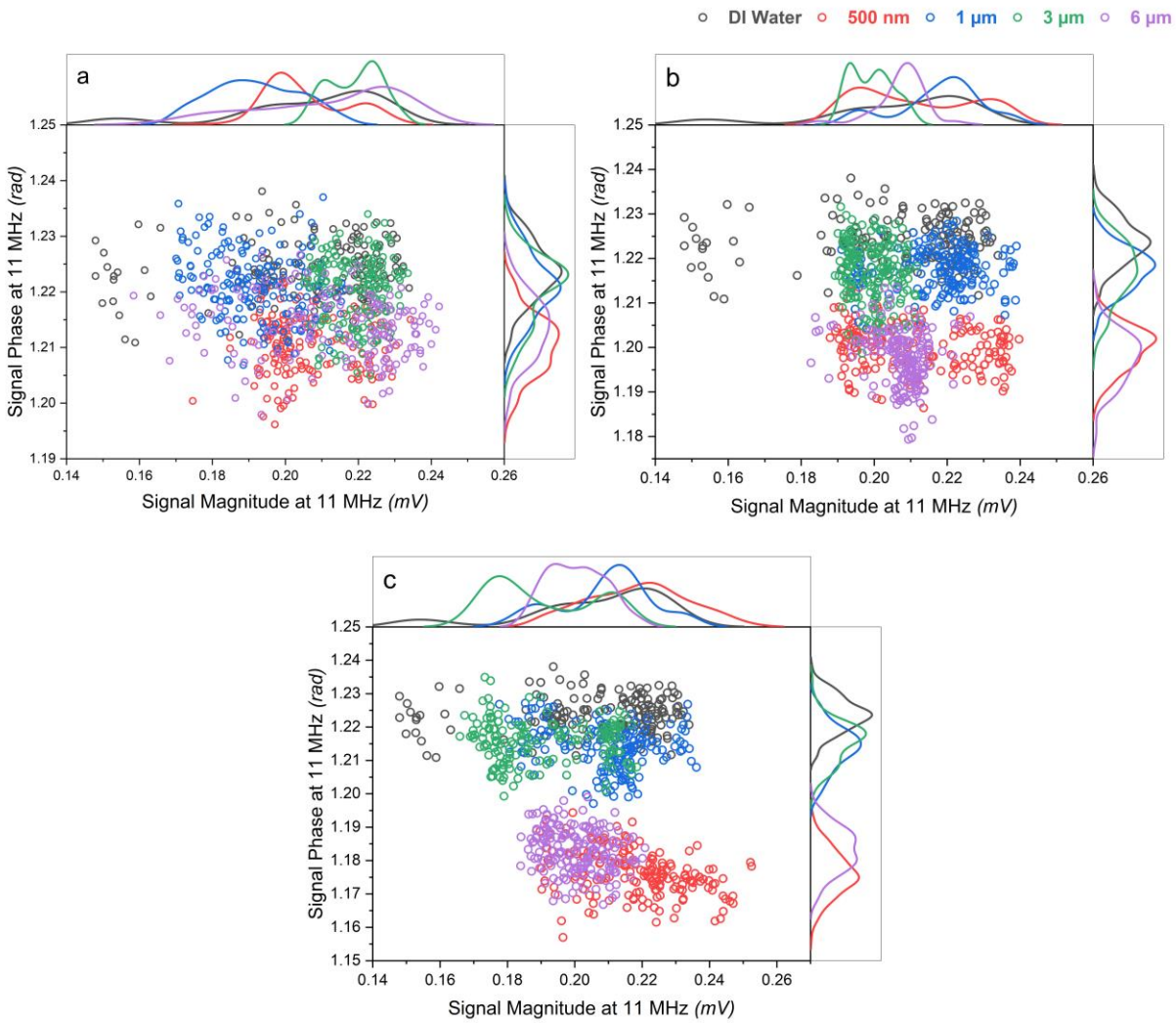

Figure 3-6. The scatter plot with the marginal histogram of all the peaks detected at 11 MHz for different concentrations of a) 0.05%, b) 0.10%, and c) 0.20% solid particle.

increases, particularly for 500 nm and 6 µm particles. This is the inverse of the behaviour observed at 4.4 MHz. At this frequency, the behaviour of 1 and 3 µm particles are identical, as is the behaviour of 500 nm and 6 µm particles.

Figure 3-6 illustrates all of the 11 MHz observations for various microparticle sizes at each concentration. The divergence from DI water for the microparticle-containing samples is less than the measurements of 4.4 MHz. In contrast to what was observed at 4.4 MHz, the addition of

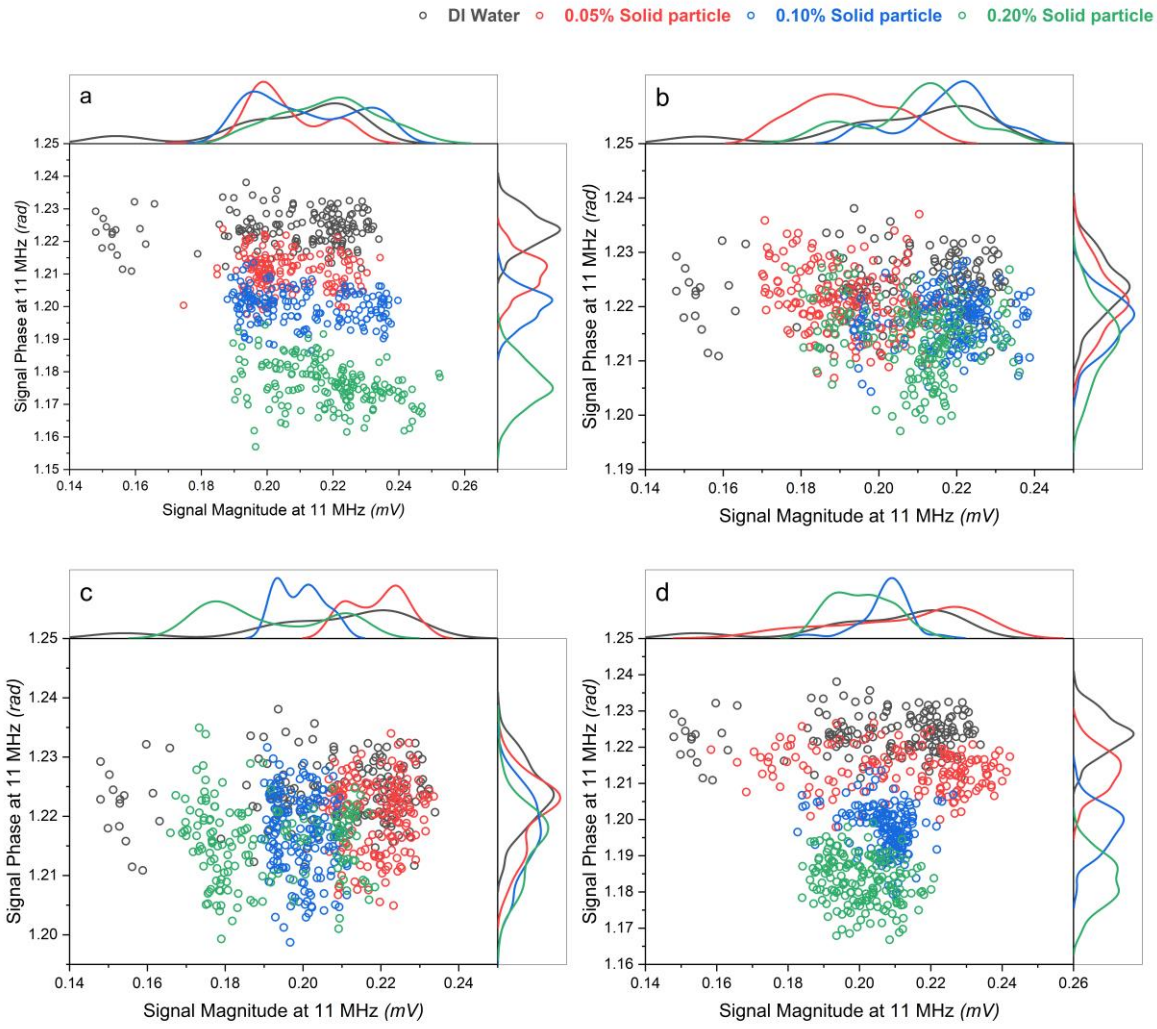

Figure 3-7. The scatter plot with the marginal histogram of all the peaks detected at 11 MHz for different particle sizes of a) 500 nm, b) 1 µm, c) 3 µm, and d) 6 µm.

microparticles reduces the signal phase, implying a less capacitive medium. 500 nm and 6 µm microparticles behave similarly, comparable to measurements at lower frequencies. The behavior of 1 µm and 3 µm microparticles is quite similar to that of pure DI water. Figure 3-7 demonstrates all of the particle size data at the middle frequency at various concentrations. In contrast to low-frequency studies, increasing the concentration decreases the signal phase for 500 nm and 6µm

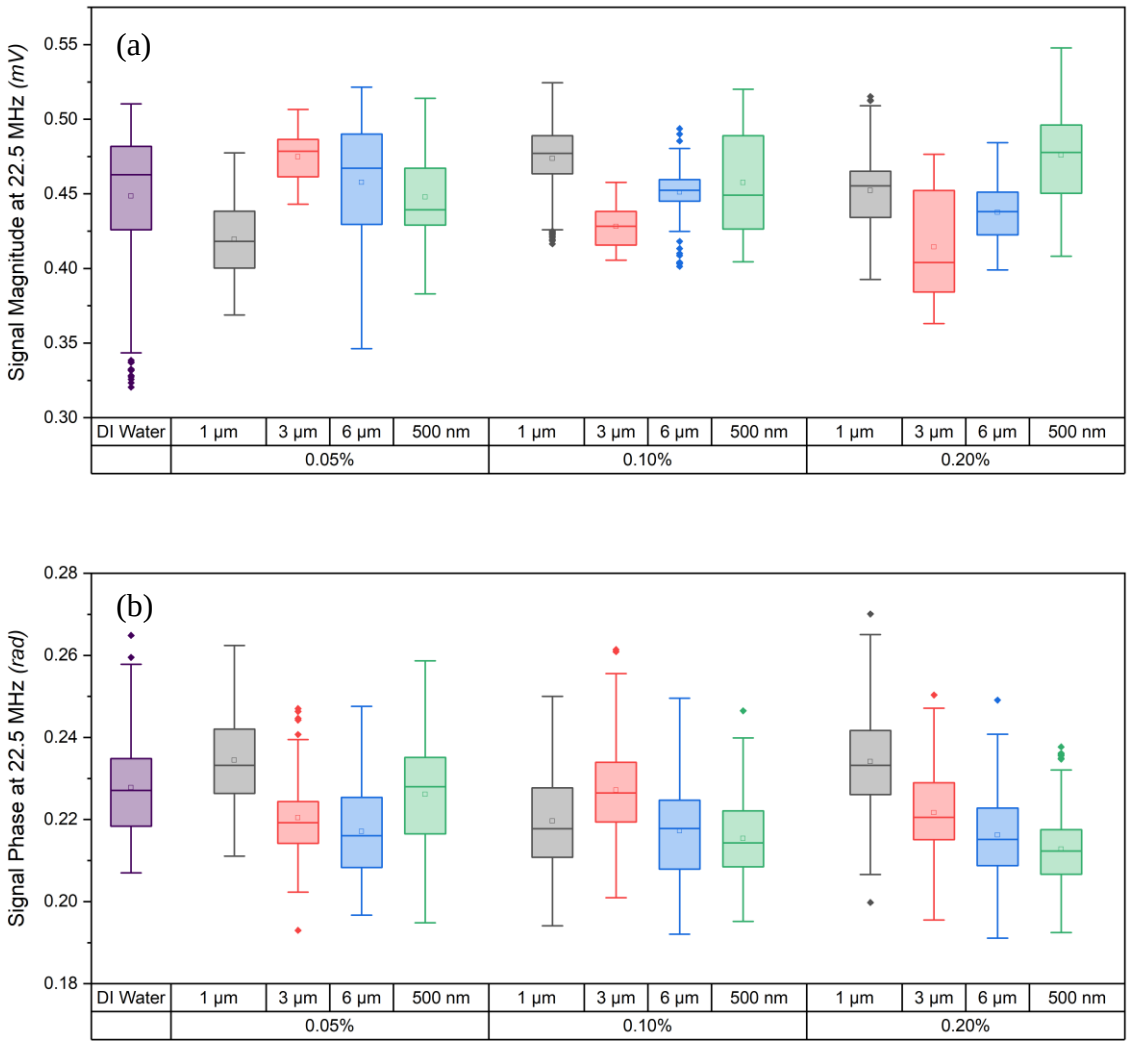

Figure 3-8. The box and whisker plot of the measurements at 22.5 MHz. (a) The signal magnitude. (b) The signal phase

microparticles. The concentration of 1 µm and 3 µm microparticles, on the other hand, appears to have little effect on the signal phase.

3.3 22.5 MHz Measurement

Figure 3-8 shows an overview of the measurements at the maximum frequency employed in this investigation, 22.5 MHz. Neither the signal's magnitude nor phase conveys any relevant trend or information.

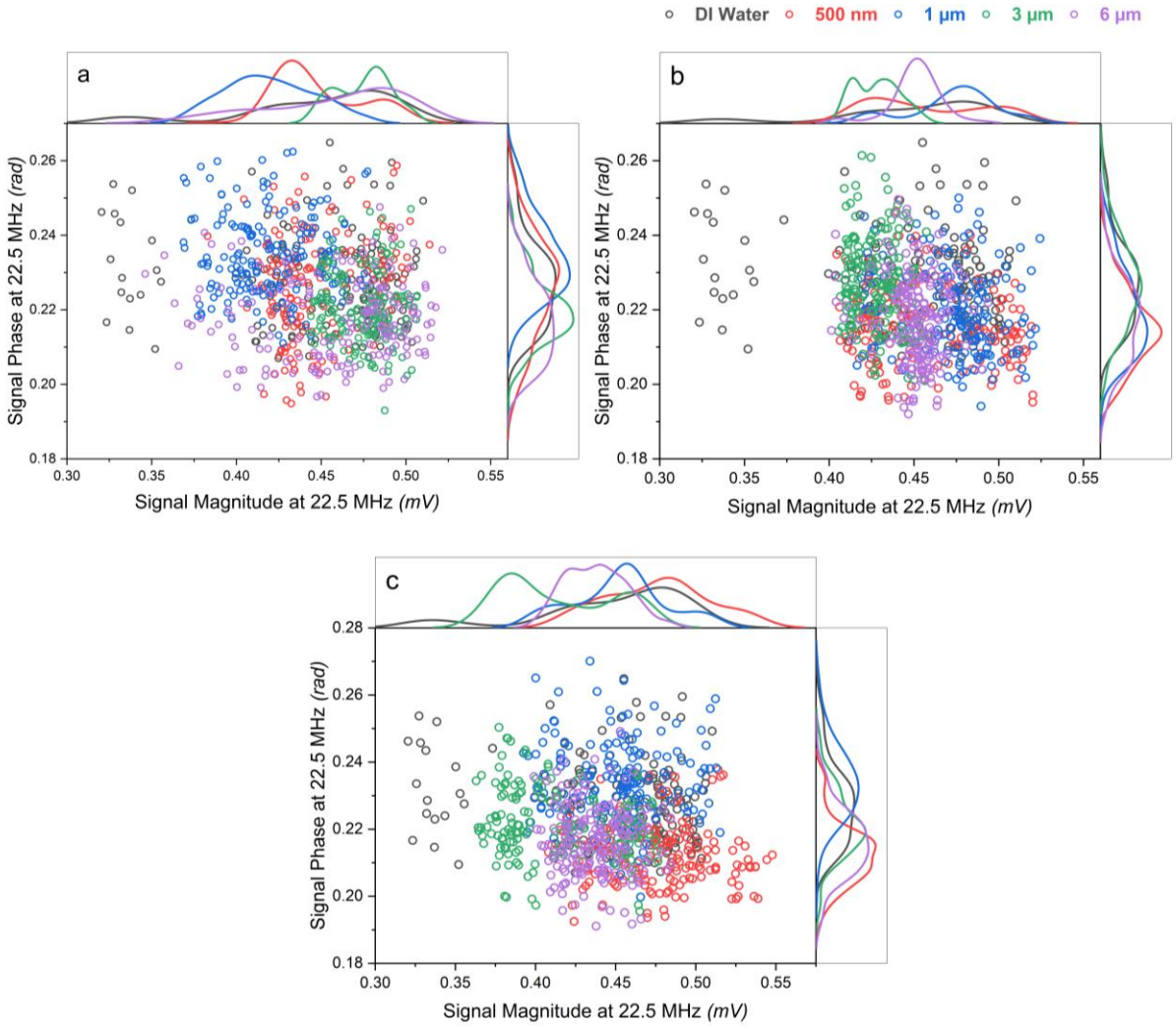

Figure 3-9. The scatter plot with the marginal histogram of all the peaks detected at 22.5 MHz for different concentrations of a) 0.05%, b) 0.10%, and c) 0.20% solid particle.

Figure 3-9 combines all of the high-frequency measurements. Readings for all concentrations and sizes are indistinguishable from pure DI water measurements. The signal phase distribution is nearly the same across all tests, resulting in a single cluster of entangled data for high-pressure measurements. Because this dataset contains no visually significant information, it was sufficient to depict the outcomes of various microparticles at each concentration.

Chapter 4: Discussion

4.1 Statistical Analysis

ANOVA was performed on the experimental findings to determine the effect of each factor and its potential interactions. OriginLab was used to do the ANOVA. The research was limited to low and medium frequencies because high frequencies could not provide a visually discernible trend. Because data normality is required for the ANOVA test, the data were subjected to the Shapiro-Wilk test prior to analysis. The results revealed that only the phase samples were drawn from a normally distributed population. Consequently, only phase measurements were included in the ANOVA.

4.1.1 ANOVA on 4.4 MHz Measurements

A two-way ANOVA was used to compare the effect of solid particle size and concentration on the signal phase at 4.4 MHz. According to the results of the two-way ANOVA, there is a statistically significant difference in signal phase between at least two levels of both factors. Furthermore, the interaction between size and concentration is significant at alpha=0.5. The overall detail of the two-way ANOVA is shown in Table 4-1.

Table 4-1. The overall result of two-way ANOVA at 4.4 MHz.

	DF	*Sum of Squares*	*Mean Square*	*F Value*	*P Value*
Size	3	1.43	4.78E-01	6019.74	<0.00001
Concentration	2	0.65	3.27E-01	4110.13	<0.00001
Interaction	6	0.28	4.59E-02	577.95	<0.00001
Model	11	2.42	2.20E-01	2774.38	<0.00001
Error	2024	0.16	7.95E-05		
Corrected Total	2035	2.59			

Tukey's HSD Test for multiple comparisons discovered that the mean value of the signal phase differed significantly between all concentration levels. Table 4-2 summarizes the mean comparison of concentrations.

Table 4-2. Tukey's HSD test for the factor of concentration at 4.4 MHz.

	MeanDiff	*SEM*	*q Value*	*Prob*	*Alpha*	*Sig*	*LCL*	*UCL*
0.10% 0.05%	1.52E-02	4.85E-04	44.263	3.33E-16	0.05	1	1.40E-02	1.63E-02
0.20% 0.05%	4.48E-02	4.85E-04	130.417	3.33E-16	0.05	1	4.36E-02	4.59E-02
0.20% 0.10%	2.96E-02	4.81E-04	86.910	3.33E-16	0.05	1	2.85E-02	3.07E-02

Tukey's comparison test between size levels, on the other hand, suggests that the mean similarity between 6 µm and 500 nm microparticles cannot be rejected. The remaining pairwise comparisons show substantial variations in mean value. Table 2 summarizes the size comparison.

Table 4-3. Tukey's HSD test for the factor of size at 4.4 MHz.

	MeanDiff	*SEM*	*q Value*	*Prob*	*Alpha*	*Sig*	*LCL*	*UCL*
1 µm 500 nm	-5.33E-02	5.55E-04	136.00	2.22E-16	0.05	1	-5.48E-02	-5.19E-02
3 µm 500 nm	-5.62E-02	5.61E-04	141.62	2.22E-16	0.05	1	-5.76E-02	-5.47E-02
3 µm 1 µm	-2.83E-03	5.58E-04	7.19	2.22E-06	0.05	1	-4.27E-03	-1.40E-03
6 µm 500 nm	-1.21E-03	5.60E-04	3.05	0.13567	0.05	0	-2.65E-03	2.31E-04
6 µm 1 µm	5.21E-02	5.57E-04	132.45	2.22E-16	0.05	1	5.07E-02	5.36E-02
6 µm 3 µm	5.50E-02	5.63E-04	138.10	2.22E-16	0.05	1	5.35E-02	5.64E-02

Tukey's test on the interaction demonstrates that for three pairs, the hypothesis of mean equality cannot be rejected: 500 nm and 6 µm microparticles at 0.05%, 1 µm and 3 µm microparticles at 0.05%, and 1 µm and 3 µm microparticles at 0.10%. The results of the interaction analysis are summarized in table 3. Means that do not share a letter differ significantly.

Table 4-4. Tukey's HSD test for the interactions at 4.4 MHz.

Size	*Concentration*	*Mean*	*Groups*								
500 nm	0.20%	0.93807	A								
6 µm	0.20%	0.92578		B							
6 µm	0.10%	0.88990			C						
500 nm	0.10%	0.88131				D					
500 nm	0.05%	0.86165					E				
6 µm	0.05%	0.86156					E				
1 µm	0.20%	0.85134						F			
3 µm	0.20%	0.84640							G		
1 µm	0.10%	0.83938								H	
3 µm	0.10%	0.83717								H	
1 µm	0.05%	0.83341									I
3 µm	0.05%	0.83195									I

The signal phase interaction plot for both variables at 4.4 MHz is shown in Figure 4-1. Figure 4-1(a) indicates that at low concentrations, 1 and 3 µm microparticles have the same mean, as do 500 nm and 6 µm microparticles. The overall trend of mean values for 1 and 3 µm microparticles is comparable, as is the overall trend of mean values for 500 nm and 6 µm microparticles. Tukey's test on size shows that 1 and 3 µm microparticles have different impacts on the signal phase; however, this effect is only detectable at concentrations greater than 0.20%. The trend lines of 500 nm and 6 µm microparticles converge at this point. This indicates that an increase in the concentration of small particles may interfere with the signal phase. Figure 4-1(b) shows that an increase in concentration, regardless of particle size, will surely increase the signal phase.

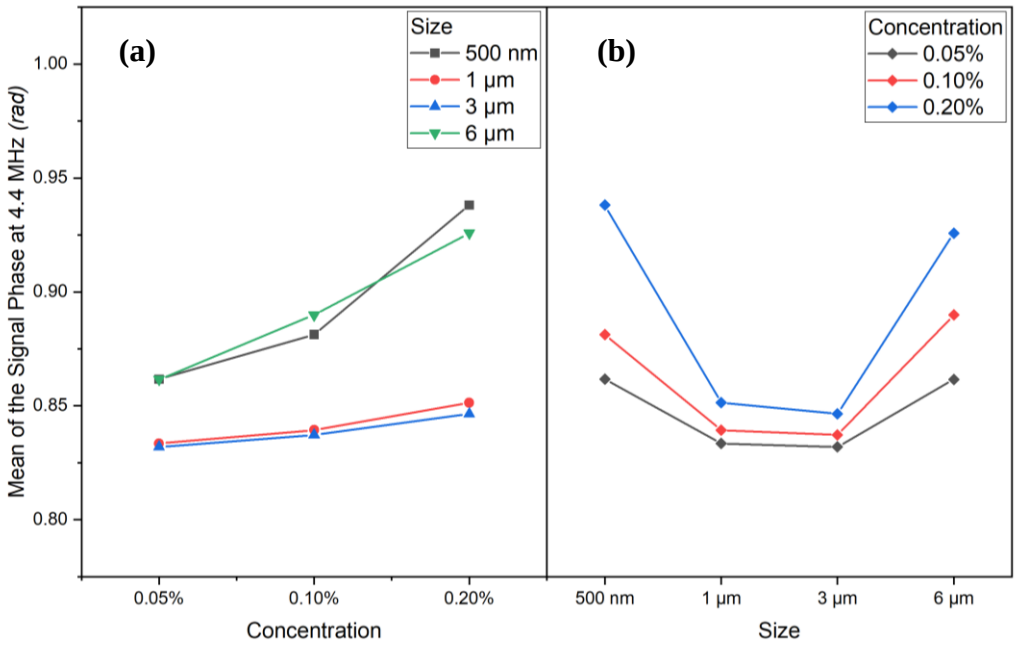

Figure 4-1. (a) The interaction plot for the factor of concentration at 4.4 MHz. (b) The interaction plot for the factor of size at 4.4 MHz.

4.1.2 ANOVA on 11 MHz Measurements

The impact of solid particle size and concentration on the phase of the 11 MHz signals was compared using a two-way ANOVA. The two-way ANOVA shows that there is a noticeable shift in signal phase between any two levels of either factor. In addition, at an alpha level of 0.5, there is a statistically significant interaction between size and concentration. Table 4-5 displays the overall results of the two-way ANOVA.

Table 4-5. The overall result of two-way ANOVA at 11 MHz.

	DF	*Sum of Squares*	*Mean Square*	*F Value*	*P Value*
Size	3	0.22	7.34E-02	1973.17	<0.00001
Concentration	2	0.12	6.25E-02	1679.55	<0.00001
Interaction	6	0.06	1.08E-02	289.83	<0.00001
Model	11	0.42	3.82E-02	1027.45	<0.00001
Error	2024	0.08	3.72E-05		
Corrected Total	2035	0.50			

As shown by Tukey's HSD Test for multiple comparisons, the mean of the signal phase varied significantly between concentrations. Concentration comparisons are summarized in Table 4-6.

Table 4-6. Tukey's HSD test for the factor of concentration at 11 MHz.

	MeanDiff	*SEM*	*q Value*	*Prob*	*Alpha*	*Sig*	*LCL*	*UCL*
0.10% 0.05%	-8.45E-03	3.32E-04	36.01	3.33E-16	0.05	1	-9.23E-03	-7.67E-03
0.20% 0.05%	-1.98E-02	3.32E-04	84.21	3.33E-16	0.05	1	-2.06E-02	-1.90E-02
0.20% 0.10%	-1.13E-02	3.29E-04	48.63	3.33E-16	0.05	1	-1.21E-02	-1.06E-02

However, as shown by Tukey's test of significance between size groups, it is impossible to dismiss the possibility that the means of 1 µm and 3 µm microparticles are similar. The remaining pairwise comparisons show substantial variations in mean value. The size comparison is summarized in Table 4-7.

Table 4-7. Tukey's HSD test for the factor of size at 11 MHz.

	MeanDiff	*SEM*	*q Value*	*Prob*	*Alpha*	*Sig*	*LCL*	*UCL*
1 µm 500 nm	2.24E-02	3.80E-04	83.28	2.22E-16	0.05	1	2.14E-02	2.33E-02
3 µm 500 nm	2.25E-02	3.84E-04	82.88	2.22E-16	0.05	1	2.15E-02	2.35E-02
3 µm 1 µm	1.45E-04	3.81E-04	0.54	0.98122	0.05	0	-8.35E-04	1.13E-03
6 µm 500 nm	2.42E-03	3.83E-04	8.95	1.51E-09	0.05	1	1.44E-03	3.41E-03
6 µm 1 µm	-1.99E-02	3.81E-04	73.98	2.22E-16	0.05	1	-2.09E-02	-1.90E-02
6 µm 3 µm	-2.01E-02	3.85E-04	73.69	2.22E-16	0.05	1	-2.11E-02	-1.91E-02

Tukey's test reveals that the level of interaction is greater at 11 MHz than at 4.4 MHz. The test hypothesis cannot be rejected by more pairs. Table 4-8 summarizes the findings from the interaction analysis. Distinct differences exist between pairs that do not share a letter.

Table 4-8. Tukey's HSD test for the interactions at 11 MHz.

Size	*Concentration*	*Mean*	*Groups*							
1 µm	0.05%	1.22108	A							
3 µm	0.05%	1.2203	A							
1 µm	0.10%	1.21746		B						
3 µm	0.10%	1.21699		B						
3 µm	0.20%	1.21565		B	C					
1 µm	0.20%	1.21383			C					
6 µm	0.05%	1.2136			C					
500 nm	0.05%	1.21048				D				
500 nm	0.10%	1.20009					E			
6 µm	0.10%	1.19755						F		
6 µm	0.20%	1.18305							G	
500 nm	0.20%	1.17616								H

Figure 4-2 depicts the signal phase interaction curve at 11 MHz for both variables. In contrast to the low-frequency results, the lines in Figure 4-2(a) have a negative slope. Similar to low-frequency studies, 1 and 3 µm microparticles respond similarly, as do 500 nm and 6 µm microparticles. The Tukey test suggests that misclassification may occur when comparing the maximum concentration of 1 and 3 µm microparticles with the lowest concentration of 6 µm microparticles. At lower frequencies, no such resemblance between the two concentration levels was found. Figure 4-2(b) illustrates that adding microparticles to the droplets consistently decreases the signal phase at 11 MHz.

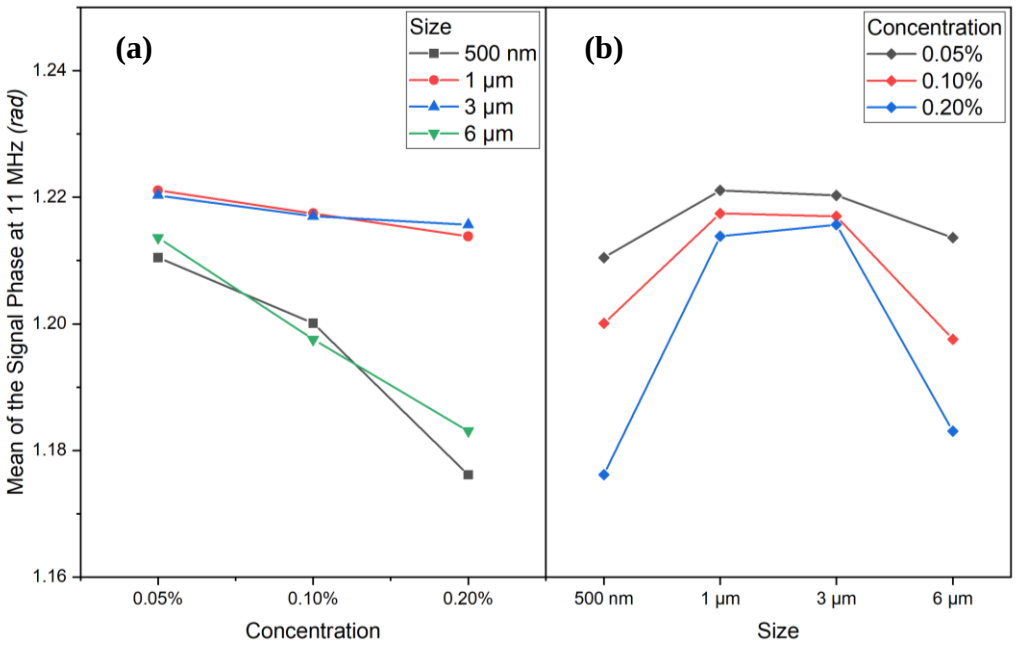

Figure 4-2. (a) The interaction plot for the factor of concentration at 11 MHz. (b) The interaction plot for the factor of size at 11 MHz.

4.1.3 Analysis of Similarities and Trends

The ANOVA test results demonstrate a significant similarity between 1 and 3 µm microparticles and 500 nm and 6 µm microparticles. Aside from that, the disparity between these two groups is too large to be coincidental. This fact was examined from a variety of perspectives, including but not limited to the device's resolution and the ability of 500 nm microparticles to cluster together. The experimental procedure was also examined. Following a thorough examination of the sample preparation procedure, it was discovered that 1 µm and 3 µm microparticles are carboxylated. Coating the microspheres with a carboxyl group increases the particle's negative surface charge [119]. A numerical study investigated the distribution state of an ion solution medium and droplet dynamics in the presence of an alternating current electric field. Ions are transferred and net charges are generated by electric fields. The influence of net charges on medium polarization and

electric field force Positive and negative ion migration modifies the charge balance of the solution. Positive-negative ion concentrations are followed by net charges. The net charge, like the polarization charge, influences the electric field, strengthening or weakening it based on its location [120]. As a result, the presence of negatively charged polystyrene beads altered both the polarization of the droplets and the electric field itself, resulting in a decrease in the dipole moment of the media as compared to the presence of inert polystyrene beads.

The electrical conductivity of polystyrene microbeads is much lower than that of DI water. As a result, the inclusion of polystyrene microparticles reduces the media's conductivity. A numerical investigation of the electrical impedance measurement of droplets in a thin-walled glass capillary revealed that as the media conductivity decreases, the maximum phase measurements move to lower frequencies, as illustrated in figure 1 [121]. This is consistent with the measurement used in this investigation. For all concentrations, 4.4 MHz is put on the left side of the peak in this study. As a result, an increase in microparticle concentration, which leads to a decrease in conductivity, would increase the signal phase. The 11 MHz data, on the other hand, are on the right side of the peak. As a result, the inclusion of microparticles reduces the signal phase.

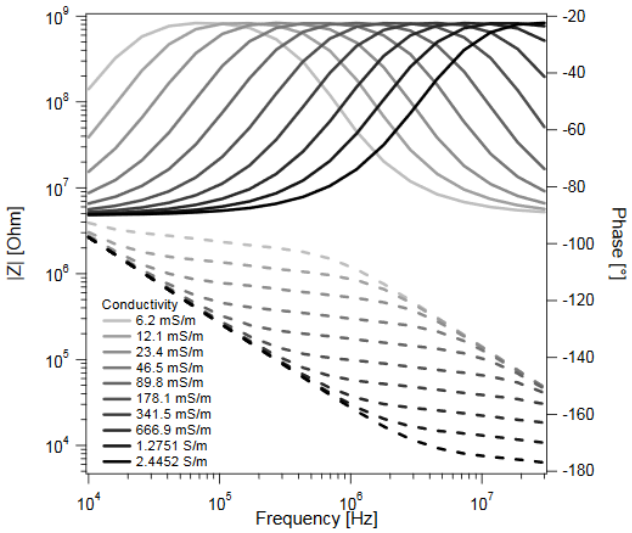

Figure 4-3. The upper curves show the phase angle's frequency dependency for liquid conductivities ranging from 6.2 mS/m to 2.4452 S/m. The lower graphs illustrate the frequency dependence of the impedance modulus for liquid conductivities ranging from 6.2 mS/m to 2.4452 S/m; with permission [121]**.**

4.2 KNN Classification

The k-Nearest Neighbor algorithm is used to classify the sample categories used in this study and to define the sensor's sensitivity. Initially, all of the categories contained in the experiment are utilized for classification without any alterations, and then, based on the classification findings and 4.1, adjustments are made to determine the proper use of the sensor. Only the signal phase at low and medium frequencies is considered for all classifications. The KNN parameters are Euclidean distance with no weight, ten nearest neighbours for categorizing each point, and five folds for cross-validation.

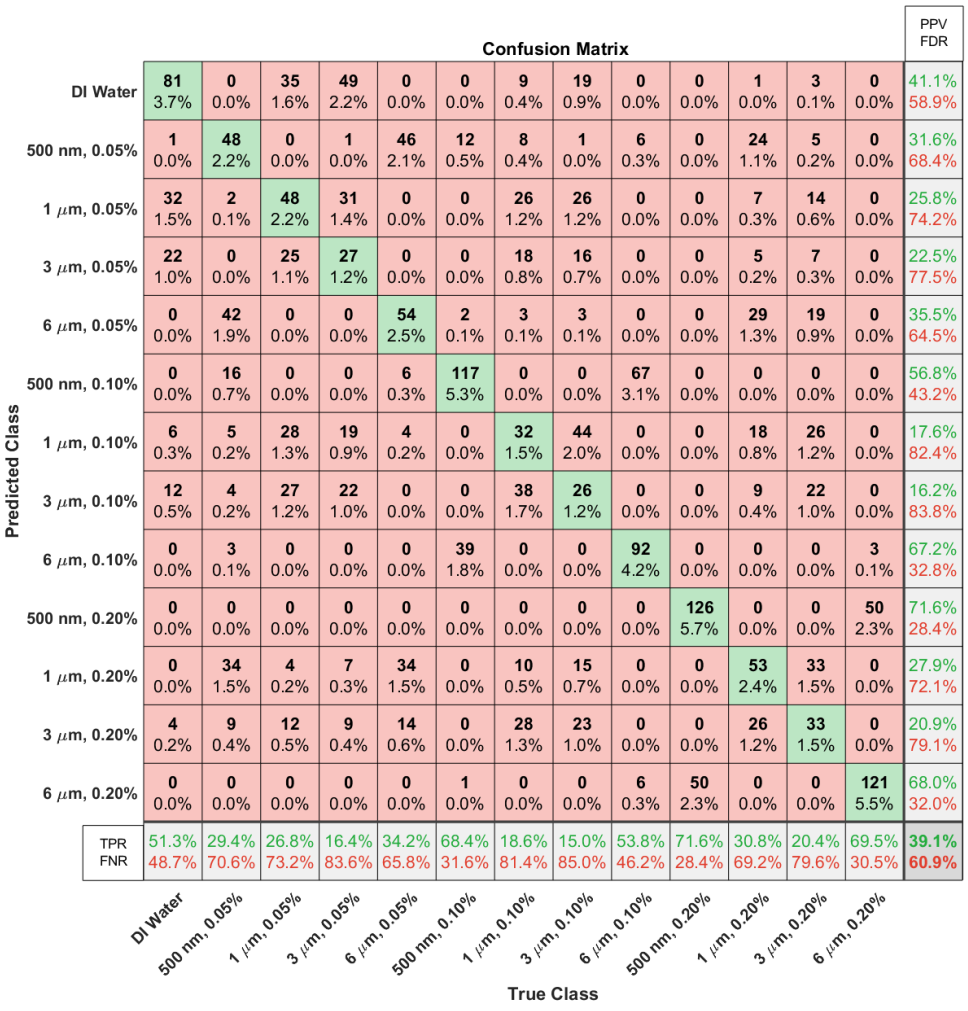

Figure 4-4. The first KNN model used with 13 different categories.

Figure 4-4 depicts the outcome of the first KNN model. According to the confusion matrix, the model performs extremely poorly at 1 and 3 µm. These two microparticles are frequently mislabeled as the same, both at the same and different concentrations. The model's performance for detecting 1 µm and 3 µm microparticles increases with increasing concentration but remains unsatisfactory. This is consistent with the results of the ANOVA test in 4.1. For 500 nm and 6 µm microparticles, the KNN model performs substantially better, especially at greater concentrations. At lower frequencies, 500 nm and 6 µm microparticles are frequently confused. The ANOVA test

likewise revealed the resemblance between these two microparticles at a concentration of 0.5%. The sensitivity of the sensor for this model is 39.1%.

The findings of the ANOVA and the conclusion drawn from the first model indicate that the carboxylated PS beads exhibit significantly distinct behaviours when exposed to an electric field. Because of this altered behaviour, the device will have a reduced level of sensitivity. As a result, the information in the dataset about the carboxylated group is removed, and a new model that is trained based on the non-carboxylated PS beads is developed. Figure 4-5 demonstrates that the sensitivity of the device increases to 69.7% with just this one adjustment being made. Despite this, the vast majority of incorrect classifications are made between the same concentration groups. This is due to the fact that the lines representing each particle size are so close together in Figure 4-1 and Figure 4-2. Therefore, the device's sensitivity to the change in concentration would most likely be increased as a result of this.

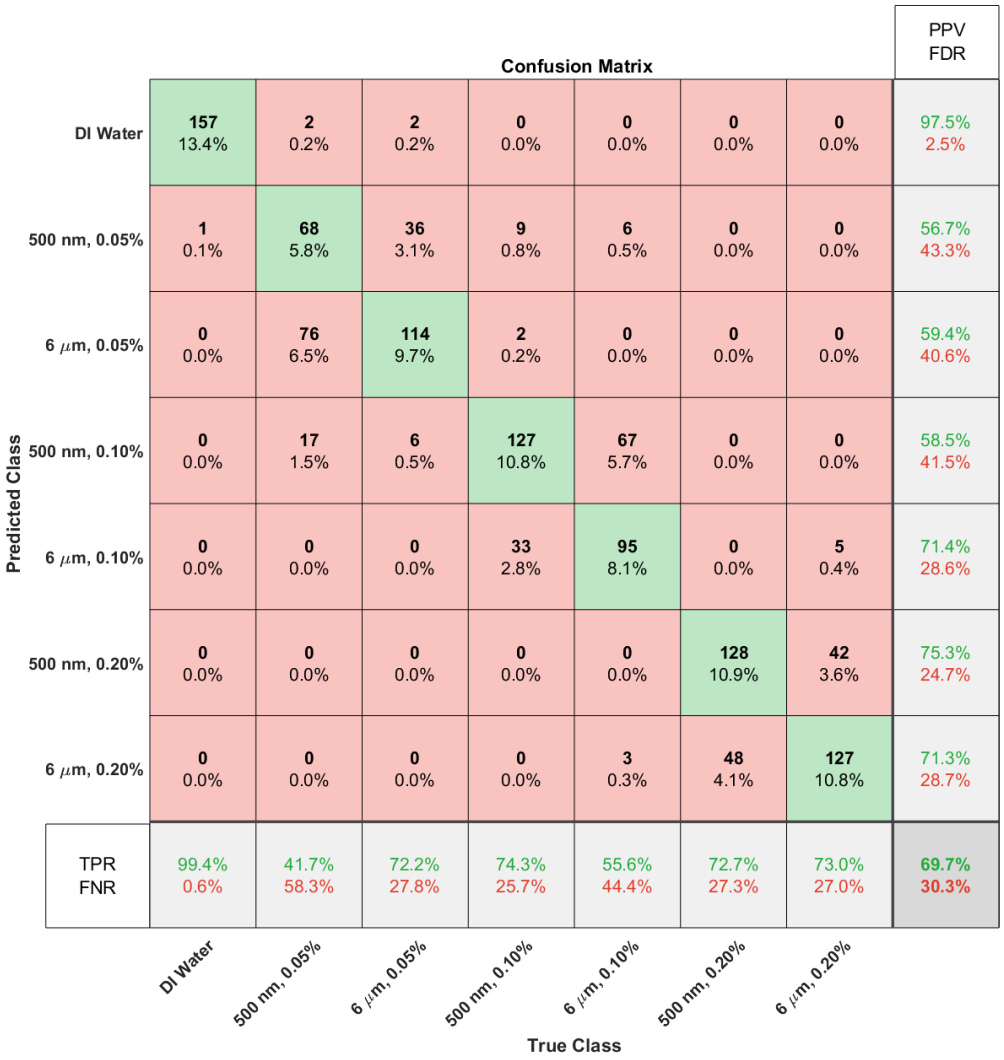

Figure 4-5. The second KNN model used with only non-carboxylated microplastics.

In the final step of the evaluation, the effectiveness of the device was evaluated based only on its ability to identify the concentration of non-carboxylated microbeads present in the droplets Figure 4-6. When the model's sole purpose is to categorize the concentration, it has a sensitivity of 95.0%. This outcome is far better than the previous two models.

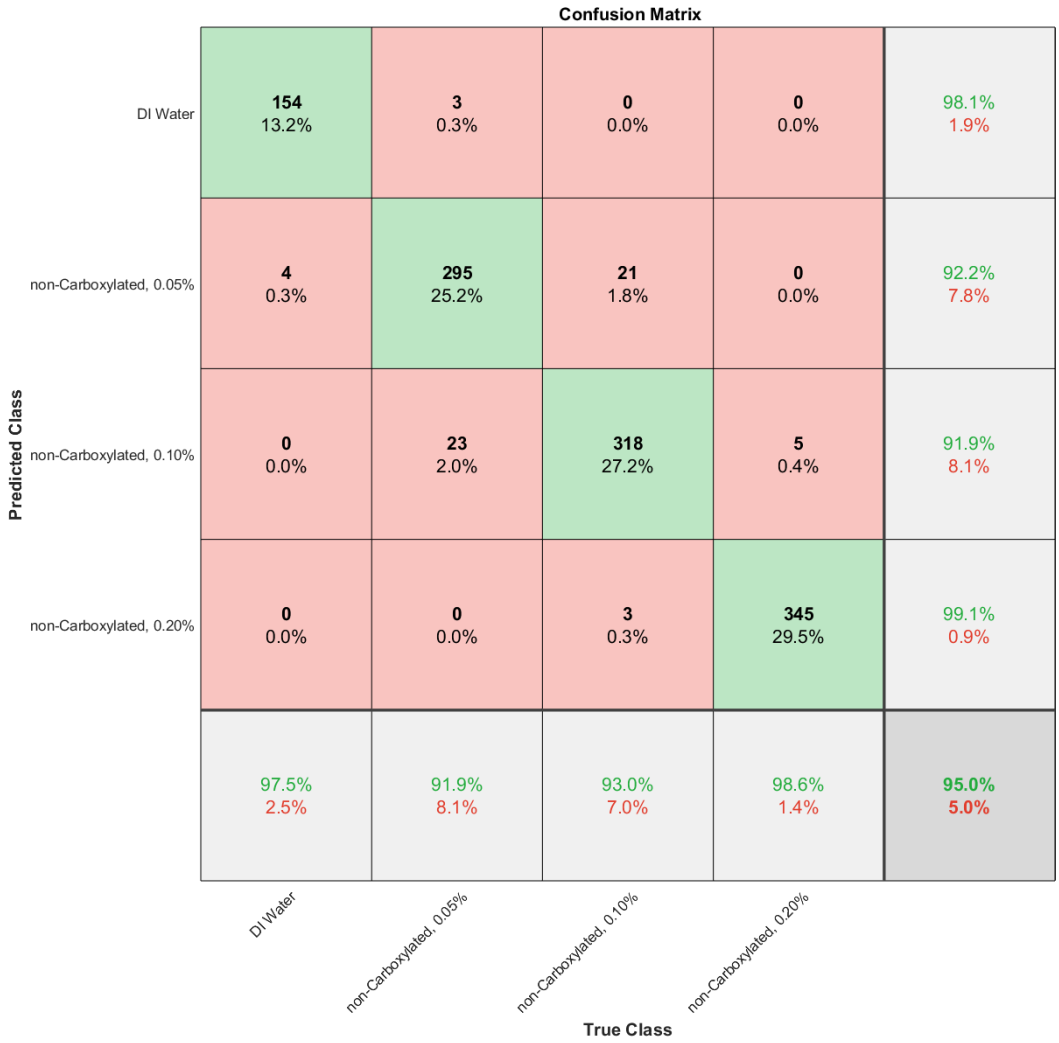

Figure 4-6. The third KNN model used to classify the concentration of non-carboxylated microplastics.

In conclusion, despite the fact that the results of the ANOVA reveal that both size and concentration are affecting the signal phase, the device is mostly sensitive to the concentration of the microplastics that are present in the droplets. This is reflected in the q-Values found in Table 4-2, Table 4-3, Table 4-6, and Table 4-7. Aside from the variations that are brought on by the carboxylation effect, the q-Value of the mean comparison of 500 and 6 µm microparticles is significantly lower than the q-Value of the comparisons that were made between concentration levels. Therefore, the primary capability of this device, which has been created using the most

straightforward method of MIFC electrode fabrication, is the ability to detect the concentration of microplastics in droplets.

4.3 Equivalent circuit model and system overview

Figure 4-7 is proposed as the equivalent circuit model in two different conditions based on the findings of the experiment. The circuit always contains three double-layer capacitors. When there is no droplet in the channel, double layers form at the oil-electrode interface (Figure 4-7a). Two of the double layers are replaced by double layers at the water-electrode interface as soon as a droplet passes over the electrodes (Figure 4-7b). The droplet-covered electrode pair measures the impedance of droplet media, while the other electrode measures the impedance of mineral oil media. The parasitic capacitance is also present in all measurements induced by the electric field between wires, PCB connections, and the gold pattern on the glass. When a droplet contains microplastics, Rd and Cd vary, resulting in a phase and magnitude that differs from that of a pure water droplet [122].

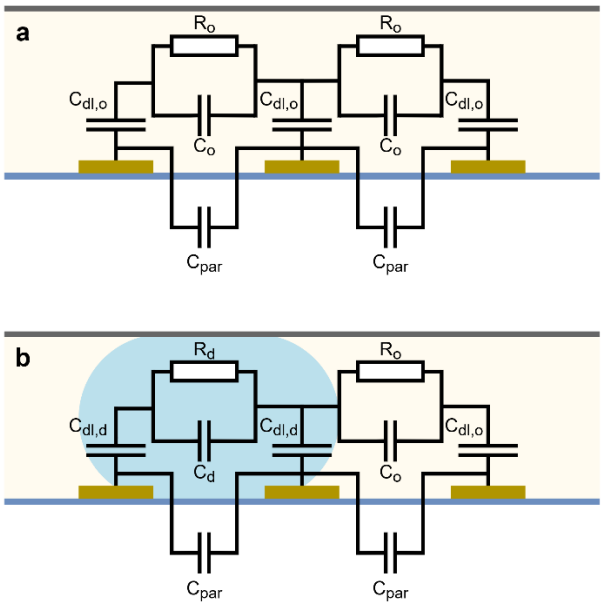

Figure 4-7. The equivalent circuit model for (a) empty channel, (b) channel with droplet

In a general sense, the capacitance of the double layer is the dominant characteristic at very low frequencies. At intermediate frequencies, the medium resistance R_d predominates the impedance measurement, and the phase rises to its highest possible value. When the frequency is increased, the medium capacitance, C_d, and the parasitic capacitance, C_{par}, begin to have a greater influence on the measured value [121].

The behaviour of non-carboxylated PS beads in droplets is depicted in Figure 4-8. This behaviour is remarkably close to the numerical simulation findings presented in Figure 4-3. According to the proposed circuit, because the difference in the peaks is not significant, the existence of the microplastic in the droplet does not modify the resistive behaviour of the media sufficiently to differentiate it. As the frequency increases, the disparity between the polylines initially grows, and eventually, they all converge with each other. This indicates that the capacitive behaviour of the droplet can be used to detect the presence of microplastics, as long as the frequency is not too high to allow the parasitic capacitance to dominate. At the lowest recorded frequency, the greatest difference between the signal phases is read. This means that the presence of microplastics will have the greatest effect on the media's double-layer capacitance. This could be because the polarity of the water molecules causes the majority of the polarization in this system. At higher frequencies, the huge water molecules may be unable to follow the pattern of the AC field. As a result, the microplastics can only disrupt the overall polarization at low frequencies.

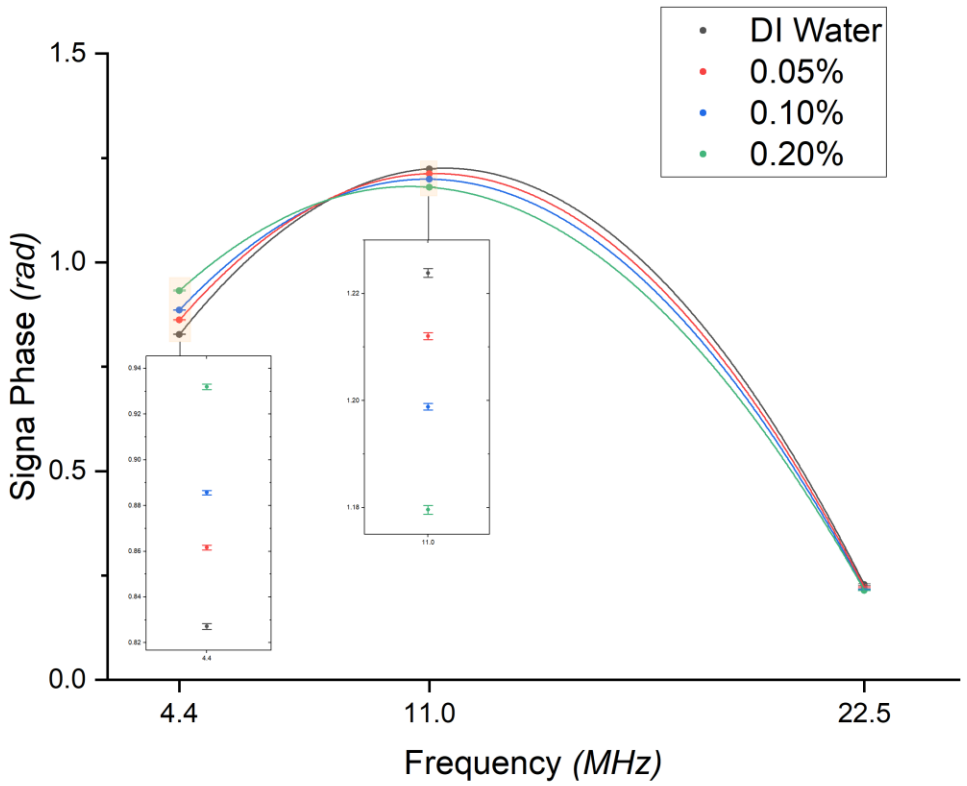

Figure 4-8. The bode plot drawn from the three frequencies measured in this research for different concentrations of non-carboxylated microplastics and DI water.

Chapter 5: Conclusion

5.1 Summary

This thesis focuses on the detection of microplastics in water droplets. To identify and quantify microplastics, we are building and analyzing a new microfluidic device based on impedance cytometry principles. The size and concentration of microplastics were detected using a flow-focusing droplet generator with coplanar electrodes. There were four distinct sizes of polystyrene microbeads utilized (500 nm, 1 µm, 3 µm, and 6 µm) with three different concentrations (0.05%, 0.10%, and 0.20% g/ml). Using a lock-in amplifier, impedance measurements were conducted at three distinct frequencies: 4,4 MHz, 11 MHz, and 22.5 MHz. ANOVA and KNN classification were used to examine the outcomes. It has been demonstrated that signal phase at low and medium frequencies discriminates sizes and concentrations most effectively. The carboxyl group on the surface of the 1 and 3 µm microbeads interfered significantly with the signal phase and nearly made the droplets containing microplastic resemble pure DI water droplets. ANOVA and KNN classification findings demonstrated that the microfluidic device is highly sensitive to the concentration of non-carboxylated polystyrene beads (500 nm and 6 µm) and can classify the concentration levels with 95.0% accuracy. At low frequencies, the presence of microplastics was discovered to increase the signal phase, whereas, at medium frequencies, it decreased the signal phase. This behaviour is a result of the poorer conductivity of microplastic-containing droplets. On the basis of a proposed equivalent circuit, it was hypothesized that the presence of microplastics in droplets can significantly alter the properties of the double-layer capacitance formed at the interface between the droplet and the electrode, making lower frequencies superior for distinguishing between different concentrations. The prevalence of parasitic capacitance at high frequencies renders observations indistinguishable. Finally, it was demonstrated that the resistive

behaviour of the droplets does not vary as much as the double-layer capacitance behaviour, rendering medium frequencies less discriminatory.

While microfluidic impedance flow cytometry has been investigated as a useful tool for detecting and evaluating microplastics, there are several limitations to this work that must be addressed. The size distribution of the microplastics employed in this study is restricted and not indicative of the real-world size distribution. To avoid clogs when testing a wider size range, the channel size must be increased. However, due to the bigger sensing zone, such an increase in the channel size will result in reduced sensitivity to small microplastics. Furthermore, the current device has been tested as a proof of concept and is not suitable for use with true aqueous solutions such as seawater due to the electrochemical corrosion of the electrodes in the current design.

5.2 Contributions

We employed microfluidic impedance flow cytometry to explore the influence of microplastic concentration, size, and surface functionalization on water droplets in this study. Our findings provide important insights into the behaviour of microplastics in water droplets.

- We discovered that the presence of microplastics alters the electrical characteristics of water droplets greatly. Using impedance measurements, this information can be used to forecast the prevalence of microplastics in water droplets.
- We discovered that microplastic surface fictionalization has a significant impact on the electrical characteristics of droplets, essentially making the microplastics transparent to the electric field.
- To explain the experimental results, we proposed an equivalent circuit for measuring the impedance of microplastics in water droplets. Such an equivalent circuit is not confined to

microplastic detection and may be used for all theoretical studies of droplet content analysis.

5.3 Future Work

- The microplastics employed in this research had a very narrow size range. Using a broader range with larger microplastics may provide more insight into the effect of size on droplet impedance.
- The microplastics in this investigation were diluted in DI water, which was far from a realistic sample. The research can be expanded by using more realistic samples, such as tap water. A passivation layer of SiO_2 can be placed over the electrodes to prevent electrochemical corrosion.This research uncovered the effect of the carboxylate group on the surface of polystyrene beads by accident. Investigating the influence of functional groups and biological contaminations on the surface of microplastics can significantly contribute to the future of microfluidic impedance flow cytometry in microplastic detection.
- Both the continuous phase and the dispersed phase were extremely non-conductive in this study. The conductivity of both of these phases can be evaluated to determine their effect on the detection of microplastics. These conductivities can be optimized to get the best signal-to-noise ratio.
- According to the ANOVA results, the size of the microparticles influences the signal phase. However, our coplanar electrodes were insufficiently advanced to detect this impact. Other configurations of electrodes can also be evaluated for their sensitivity to size fluctuation.

Bibliography

[1] A. Lusher, *Microplastics in the marine environment: Distribution, interactions and effects*. Springer International Publishing, 2015. doi: 10.1007/978-3-319-16510-3_10/FIGURES/1.

[2] A. A. Koelmans, E. Besseling, and W. J. Shim, *Nanoplastics in the aquatic environment. Critical review*. Springer International Publishing, 2015. doi: 10.1007/978-3-319-16510-3_12/FIGURES/3.

[3] P. Kershaw, *Sources, fate and effects of microplastics in the marine environment: a global assessment*. International Maritime Organization, 2015. Accessed: Sep. 07, 2022. [Online]. Available: http://localhost:8080/xmlui/handle/123456789/735

[4] A. A. Koelmans, N. H. Mohamed Nor, E. Hermsen, M. Kooi, S. M. Mintenig, and J. de France, "Microplastics in freshwaters and drinking water: Critical review and assessment of data quality," *Water Res*, vol. 155, pp. 410–422, May 2019, doi: 10.1016/J.WATRES.2019.02.054.

[5] A. A. Koelmans, P. E. Redondo-Hasselerharm, N. H. M. Nor, V. N. de Ruijter, S. M. Mintenig, and M. Kooi, "Risk assessment of microplastic particles," *Nature Reviews Materials 2022 7:2*, vol. 7, no. 2, pp. 138–152, Jan. 2022, doi: 10.1038/s41578-021-00411-y.

[6] M. Kooi, A. K.-E. S. & Technology, and undefined 2019, "Simplifying microplastic via continuous probability distributions for size, shape, and density," *ACS Publications*, vol. 6, no. 9, pp. 551–557, Sep. 2019, doi: 10.1021/acs.estlett.9b00379.

[7] L. Cabernard, L. Roscher, C. Lorenz, G. Gerdts, and S. Primpke, "Comparison of Raman and Fourier Transform Infrared Spectroscopy for the Quantification of Microplastics in the Aquatic Environment," *Environ Sci Technol*, vol. 52, no. 22, pp. 13279–13288, Nov. 2018,

doi: 10.1021/ACS.EST.8B03438/ASSET/IMAGES/LARGE/ES-2018-03438R_0004.JPEG.

[8] D. Schymanski, C. Goldbeck, H. U. Humpf, and P. Fürst, "Analysis of microplastics in water by micro-Raman spectroscopy: Release of plastic particles from different packaging into mineral water," *Water Res*, vol. 129, pp. 154–162, Feb. 2018, doi: 10.1016/J.WATRES.2017.11.011.

[9] C. Li, R. Busquets, and L. C. Campos, "Assessment of microplastics in freshwater systems: A review," *Science of The Total Environment*, vol. 707, p. 135578, Mar. 2020, doi: 10.1016/J.SCITOTENV.2019.135578.

[10] N. Zhang, Y. bin Li, H. R. He, J. F. Zhang, and G. S. Ma, "You are what you eat: Microplastics in the feces of young men living in Beijing," *Science of The Total Environment*, vol. 767, p. 144345, May 2021, doi: 10.1016/J.SCITOTENV.2020.144345.

[11] Y. S. Ibrahim *et al.*, "Detection of microplastics in human colectomy specimens," *JGH Open*, vol. 5, no. 1, pp. 116–121, Jan. 2021, doi: 10.1002/JGH3.12457.

[12] H. A. Leslie, M. J. M. van Velzen, S. H. Brandsma, A. D. Vethaak, J. J. Garcia-Vallejo, and M. H. Lamoree, "Discovery and quantification of plastic particle pollution in human blood," *Environ Int*, vol. 163, p. 107199, May 2022, doi: 10.1016/J.ENVINT.2022.107199.

[13] Y. K. Song *et al.*, "A comparison of microscopic and spectroscopic identification methods for analysis of microplastics in environmental samples," *Mar Pollut Bull*, vol. 93, no. 1–2, pp. 202–209, Apr. 2015, doi: 10.1016/J.MARPOLBUL.2015.01.015.

[14] W. Fu, J. Min, W. Jiang, Y. Li, and W. Zhang, "Separation, characterization and identification of microplastics and nanoplastics in the environment," *Science of The Total Environment*, vol. 721, p. 137561, Jun. 2020, doi: 10.1016/J.SCITOTENV.2020.137561.

[15] V. Stock *et al.*, “Impact of artificial digestion on the sizes and shapes of microplastic particles,” *Food and Chemical Toxicology*, vol. 135, p. 111010, Jan. 2020, doi: 10.1016/J.FCT.2019.111010.

[16] V. C. Shruti, F. Pérez-Guevara, P. D. Roy, and G. Kutralam-Muniasamy, “Analyzing microplastics with Nile Red: Emerging trends, challenges, and prospects,” *J Hazard Mater*, vol. 423, p. 127171, Feb. 2022, doi: 10.1016/J.JHAZMAT.2021.127171.

[17] M. Blevins *et al.*, “Field-Portable Microplastic Sensing in Aqueous Environments: A Perspective on Emerging Techniques,” *Sensors*, vol. 21, no. 10, p. 3532, May 2021, doi: 10.3390/s21103532.

[18] M. Tamminga and E. K. Fischer, “Microplastics in a deep, dimictic lake of the North German Plain with special regard to vertical distribution patterns,” *Environmental Pollution*, vol. 267, p. 115507, Dec. 2020, doi: 10.1016/J.ENVPOL.2020.115507.

[19] H. A. Nel *et al.*, “Citizen science reveals microplastic hotspots within tidal estuaries and the remote Scilly Islands, United Kingdom,” *Mar Pollut Bull*, vol. 161, p. 111776, Dec. 2020, doi: 10.1016/J.MARPOLBUL.2020.111776.

[20] J. C. Prata *et al.*, “Microplastics and fibers from three areas under different anthropogenic pressures in Douro river,” *Science of The Total Environment*, vol. 776, p. 145999, Jul. 2021, doi: 10.1016/J.SCITOTENV.2021.145999.

[21] E. Hengstmann, E. Weil, P. C. Wallbott, M. Tamminga, and E. K. Fischer, “Microplastics in lakeshore and lakebed sediments – External influences and temporal and spatial variabilities of concentrations,” *Environ Res*, vol. 197, p. 111141, Jun. 2021, doi: 10.1016/J.ENVRES.2021.111141.

[22] A. Patchaiyappan *et al.*, “Prevalence of microplastics in the sediments of Odisha beaches, southeastern coast of India,” *Mar Pollut Bull*, vol. 167, p. 112265, Jun. 2021, doi: 10.1016/J.MARPOLBUL.2021.112265.

[23] X. Ji *et al.*, “Transport and fate of microplastics from riverine sediment dredge piles: Implications for disposal,” *J Hazard Mater*, vol. 404, p. 124132, Feb. 2021, doi: 10.1016/J.JHAZMAT.2020.124132.

[24] G. Grause, Y. Kuniyasu, M. F. Chien, and C. Inoue, “Separation of microplastic from soil by centrifugation and its application to agricultural soil,” *Chemosphere*, vol. 288, Feb. 2022, doi: 10.1016/J.CHEMOSPHERE.2021.132654.

[25] X. Zhang *et al.*, “Size/shape-dependent migration of microplastics in agricultural soil under simulative and natural rainfall,” *Science of the Total Environment*, vol. 815, Apr. 2022, doi: 10.1016/J.SCITOTENV.2021.152507.

[26] J. C. Prata, J. P. da Costa, A. C. Duarte, and T. Rocha-Santos, “Suspected microplastics in Atlantic horse mackerel fish (Trachurus trachurus) captured in Portugal,” *Mar Pollut Bull*, vol. 174, Jan. 2022, doi: 10.1016/J.MARPOLBUL.2021.113249.

[27] M. Mistri, A. A. Sfriso, E. Casoni, M. Nicoli, C. Vaccaro, and C. Munari, “Microplastic accumulation in commercial fish from the Adriatic Sea,” *Mar Pollut Bull*, vol. 174, p. 113279, Jan. 2022, doi: 10.1016/J.MARPOLBUL.2021.113279.

[28] V. P. Ranjan, A. Joseph, and S. Goel, “Microplastics and other harmful substances released from disposable paper cups into hot water,” *J Hazard Mater*, vol. 404, Feb. 2021, doi: 10.1016/J.JHAZMAT.2020.124118.

[29] M. F. Diaz-Basantes, D. Nacimba-Aguirre, J. A. Conesa, and A. Fullana, “Presence of microplastics in commercial canned tuna,” *Food Chem*, vol. 385, Aug. 2022, doi: 10.1016/J.FOODCHEM.2022.132721.

[30] Y. Y. Hee, K. Weston, and S. Suratman, “The effect of storage conditions and washing on microplastic release from food and drink containers,” *Food Packag Shelf Life*, vol. 32, Jun. 2022, doi: 10.1016/J.FPSL.2022.100826.

[31] W. J. Shim, Y. K. Song, S. H. Hong, and M. Jang, “Identification and quantification of microplastics using Nile Red staining,” *Mar Pollut Bull*, vol. 113, no. 1–2, pp. 469–476, Dec. 2016, doi: 10.1016/J.MARPOLBUL.2016.10.049.

[32] M. B. Ahmed *et al.*, “Microplastic particles in the aquatic environment: A systematic review,” *Science of the Total Environment*, vol. 775, Jun. 2021, doi: 10.1016/J.SCITOTENV.2021.145793.

[33] E. Fries, J. H. Dekiff, J. Willmeyer, M. T. Nuelle, M. Ebert, and D. Remy, “Identification of polymer types and additives in marine microplastic particles using pyrolysis-GC/MS and scanning electron microscopy,” *Environmental Sciences: Processes and Impacts*, vol. 15, no. 10, pp. 1949–1956, Oct. 2013, doi: 10.1039/C3EM00214D.

[34] M. Fischer and B. M. Scholz-Böttcher, “Simultaneous Trace Identification and Quantification of Common Types of Microplastics in Environmental Samples by Pyrolysis-Gas Chromatography-Mass Spectrometry,” *Environ Sci Technol*, vol. 51, no. 9, pp. 5052–5060, May 2017, doi: 10.1021/ACS.EST.6B06362/ASSET/IMAGES/LARGE/ES-2016-06362U_0003.JPEG.

[35] I. v. Kirstein *et al.*, “Drinking plastics? – Quantification and qualification of microplastics in drinking water distribution systems by µFTIR and Py-GCMS,” *Water Res*, vol. 188, Jan. 2021, doi: 10.1016/J.WATRES.2020.116519.

[36] C. Rauert *et al.*, “Concentrations of Tire Additive Chemicals and Tire Road Wear Particles in an Australian Urban Tributary,” *Environ Sci Technol*, vol. 56, no. 4, pp. 2421–2431, Feb. 2022, doi: 10.1021/ACS.EST.1C07451.

[37] L. Roscher *et al.*, “Microplastics in two German wastewater treatment plants: Year-long effluent analysis with FTIR and Py-GC/MS,” *Science of the Total Environment*, vol. 817, Apr. 2022, doi: 10.1016/J.SCITOTENV.2021.152619.

[38] K. Chouchene, T. Nacci, F. Modugno, V. Castelvetro, and M. Ksibi, “Soil contamination by microplastics in relation to local agricultural development as revealed by FTIR, ICP-MS and pyrolysis-GC/MS,” *Environmental Pollution*, vol. 303, Jun. 2022, doi: 10.1016/J.ENVPOL.2022.119016.

[39] X. X. Zhou *et al.*, “Quantitative analysis of polystyrene and poly(methyl methacrylate) nanoplastics in tissues of aquatic animals,” *Environ Sci Technol*, vol. 55, no. 5, pp. 3032–3040, Mar. 2021, doi: 10.1021/ACS.EST.0C08374.

[40] C. Dessì *et al.*, “Plastics contamination of store-bought rice,” *J Hazard Mater*, vol. 416, Aug. 2021, doi: 10.1016/J.JHAZMAT.2021.125778.

[41] M. G. J. Löder and G. Gerdts, “Methodology used for the detection and identification of microplastics—a critical appraisal,” in *Marine Anthropogenic Litter*, Springer International Publishing, 2015, pp. 201–227. doi: 10.1007/978-3-319-16510-3_8/FIGURES/7.

[42] J. Li, H. Liu, and J. Paul Chen, “Microplastics in freshwater systems: A review on occurrence, environmental effects, and methods for microplastics detection,” *Water Res*, vol. 137, pp. 362–374, Jun. 2018, doi: 10.1016/J.WATRES.2017.12.056.

[43] J. P. Harrison, J. J. Ojeda, and M. E. Romero-González, “The applicability of reflectance micro-Fourier-transform infrared spectroscopy for the detection of synthetic microplastics in marine sediments,” *Science of The Total Environment*, vol. 416, pp. 455–463, Feb. 2012, doi: 10.1016/J.SCITOTENV.2011.11.078.

[44] D. Huang *et al.*, “The occurrence and abundance of microplastics in surface water and sediment of the West River downstream, in the south of China,” *Science of The Total Environment*, vol. 756, p. 143857, Feb. 2021, doi: 10.1016/J.SCITOTENV.2020.143857.

[45] C. Villanova-Solano *et al.*, “Microplastic pollution in sublittoral coastal sediments of a North Atlantic island: The case of La Palma (Canary Islands, Spain),” *Chemosphere*, vol. 288, p. 132530, Feb. 2022, doi: 10.1016/J.CHEMOSPHERE.2021.132530.

[46] Y. Terzi, K. Gedik, A. R. Eryaşar, R. Ç. Öztürk, A. Şahin, and F. Yılmaz, “Microplastic contamination and characteristics spatially vary in the southern Black Sea beach sediment and sea surface water,” *Mar Pollut Bull*, vol. 174, p. 113228, Jan. 2022, doi: 10.1016/J.MARPOLBUL.2021.113228.

[47] T. Liang *et al.*, “Distribution and potential sources of microplastics in sediments in remote lakes of Tibet, China,” *Science of The Total Environment*, vol. 806, p. 150526, Feb. 2022, doi: 10.1016/J.SCITOTENV.2021.150526.

[48] A. Vianello *et al.*, “Microplastic particles in sediments of Lagoon of Venice, Italy: First observations on occurrence, spatial patterns and identification,” *Estuar Coast Shelf Sci*, vol. 130, pp. 54–61, Sep. 2013, doi: 10.1016/J.ECSS.2013.03.022.

[49] P. Prarat and P. Hongsawat, “Microplastic pollution in surface seawater and beach sand from the shore of Rayong province, Thailand: Distribution, characterization, and ecological risk assessment,” *Mar Pollut Bull*, vol. 174, p. 113200, Jan. 2022, doi: 10.1016/J.MARPOLBUL.2021.113200.

[50] Q. Wang, C. Guan, J. Han, M. Chai, and R. Li, “Microplastics in China Sea: Analysis, status, source, and fate,” *Science of The Total Environment*, vol. 803, p. 149887, Jan. 2022, doi: 10.1016/J.SCITOTENV.2021.149887.

[51] M. Bharath K *et al.*, “Microplastics as an emerging threat to the freshwater ecosystems of Veeranam lake in south India: A multidimensional approach,” *Chemosphere*, vol. 264, p. 128502, Feb. 2021, doi: 10.1016/J.CHEMOSPHERE.2020.128502.

[52] C. Bertoldi *et al.*, “First evidence of microplastic contamination in the freshwater of Lake Guaíba, Porto Alegre, Brazil,” *Science of The Total Environment*, vol. 759, p. 143503, Mar. 2021, doi: 10.1016/J.SCITOTENV.2020.143503.

[53] Y. Li, Z. Wang, and B. Guan, “Separation and identification of nanoplastics in tap water,” *Environ Res*, vol. 204, p. 112134, Mar. 2022, doi: 10.1016/J.ENVRES.2021.112134.

[54] I. v. Kirstein *et al.*, “Drinking plastics? – Quantification and qualification of microplastics in drinking water distribution systems by µFTIR and Py-GCMS,” *Water Res*, vol. 188, p. 116519, Jan. 2021, doi: 10.1016/J.WATRES.2020.116519.

[55] Z. Zainuddin and Syuhada, “Study of Analysis Method on Microplastic Identification in Bottled Drinking Water,” *Macromol Symp*, vol. 391, no. 1, p. 1900195, Jun. 2020, doi: 10.1002/MASY.201900195.

[56] F. Yuan, H. Zhao, H. Sun, Y. Sun, J. Zhao, and T. Xia, “Investigation of microplastics in sludge from five wastewater treatment plants in Nanjing, China,” *J Environ Manage*, vol. 301, p. 113793, Jan. 2022, doi: 10.1016/J.JENVMAN.2021.113793.

[57] R. Chand, K. Kohansal, S. Toor, T. H. Pedersen, and J. Vollertsen, “Microplastics degradation through hydrothermal liquefaction of wastewater treatment sludge,” *J Clean Prod*, vol. 335, Feb. 2022, doi: 10.1016/J.JCLEPRO.2022.130383.

[58] F. Wei *et al.*, “Distribution of microplastics in the sludge of wastewater treatment plants in chengdu, China,” *Chemosphere*, vol. 287, Jan. 2022, doi: 10.1016/J.CHEMOSPHERE.2021.132357.

[59] A. Naji, M. Nuri, and A. D. Vethaak, “Microplastics contamination in molluscs from the northern part of the Persian Gulf,” *Environmental Pollution*, vol. 235, pp. 113–120, Apr. 2018, doi: 10.1016/J.ENVPOL.2017.12.046.

[60] V. Aliko *et al.*, “Plastic invasion tolling: First evaluation of microplastics in water and two crab species from the nature reserve lagoonary complex of Kune-Vain, Albania,” *Science of The Total Environment*, vol. 849, p. 157799, Nov. 2022, doi: 10.1016/J.SCITOTENV.2022.157799.

[61] R. C. Moore *et al.*, “Microplastics in beluga whale (Delphinapterus leucas) prey: An exploratory assessment of trophic transfer in the Beaufort Sea,” *Science of The Total Environment*, vol. 806, p. 150201, Feb. 2022, doi: 10.1016/J.SCITOTENV.2021.150201.

[62] P. Schwabl *et al.*, “Detection of Various Microplastics in Human Stool,” *https://doi.org/10.7326/M19-0618*, vol. 171, no. 7, pp. 453–457, Sep. 2019, doi: 10.7326/M19-0618.

[63] L. C. Jenner, J. M. Rotchell, R. T. Bennett, M. Cowen, V. Tentzeris, and L. R. Sadofsky, "Detection of microplastics in human lung tissue using μFTIR spectroscopy," *Science of the Total Environment*, vol. 831, Jul. 2022, doi: 10.1016/J.SCITOTENV.2022.154907.

[64] N. Zhang, Y. bin Li, H. R. He, J. F. Zhang, and G. S. Ma, "You are what you eat: Microplastics in the feces of young men living in Beijing," *Science of The Total Environment*, vol. 767, p. 144345, May 2021, doi: 10.1016/J.SCITOTENV.2020.144345.

[65] Y. S. Ibrahim *et al.*, "Detection of microplastics in human colectomy specimens," *JGH Open*, vol. 5, no. 1, pp. 116–121, Jan. 2021, doi: 10.1002/JGH3.12457.

[66] J. Kim *et al.*, "Development and validation of analytical methods for detecting and identifying microplastics in salts, soy sauce, and salted pollock roe," *Journal of Food Composition and Analysis*, vol. 114, p. 104856, Dec. 2022, doi: 10.1016/J.JFCA.2022.104856.

[67] M. Sivagami *et al.*, "Extraction of microplastics from commonly used sea salts in India and their toxicological evaluation," *Chemosphere*, vol. 263, p. 128181, Jan. 2021, doi: 10.1016/J.CHEMOSPHERE.2020.128181.

[68] R. W. M. G. K. Kapukotuwa, N. Jayasena, K. C. Weerakoon, C. L. Abayasekara, and R. S. Rajakaruna, "High levels of microplastics in commercial salt and industrial salterns in Sri Lanka," *Mar Pollut Bull*, vol. 174, p. 113239, Jan. 2022, doi: 10.1016/J.MARPOLBUL.2021.113239.

[69] N. S. Soltani, M. P. Taylor, and S. P. Wilson, "Quantification and exposure assessment of microplastics in Australian indoor house dust," *Environmental Pollution*, vol. 283, p. 117064, Aug. 2021, doi: 10.1016/J.ENVPOL.2021.117064.

[70] A. Torres-Agullo, A. Karanasiou, T. Moreno, and S. Lacorte, “Airborne microplastic particle concentrations and characterization in indoor urban microenvironments,” *Environmental Pollution*, vol. 308, p. 119707, Sep. 2022, doi: 10.1016/J.ENVPOL.2022.119707.

[71] V. C. Shruti, G. Kutralam-Muniasamy, F. Pérez-Guevara, P. D. Roy, and I. E. Martínez, “Occurrence and characteristics of atmospheric microplastics in Mexico City,” *Science of the Total Environment*, vol. 847, Nov. 2022, doi: 10.1016/J.SCITOTENV.2022.157601.

[72] L. Dai *et al.*, “Pollution characteristics and source analysis of microplastics in the Qiantang River in southeastern China,” *Chemosphere*, vol. 293, p. 133576, Apr. 2022, doi: 10.1016/J.CHEMOSPHERE.2022.133576.

[73] U. R. Gurjar, K. A. M. Xavier, S. P. Shukla, A. K. Jaiswar, G. Deshmukhe, and B. B. Nayak, “Microplastic pollution in coastal ecosystem off Mumbai coast, India,” *Chemosphere*, vol. 288, p. 132484, Feb. 2022, doi: 10.1016/J.CHEMOSPHERE.2021.132484.

[74] Y. Fan *et al.*, “Spatiotemporal dynamics of microplastics in an urban river network area,” *Water Res*, vol. 212, p. 118116, Apr. 2022, doi: 10.1016/J.WATRES.2022.118116.

[75] Q. Wang, C. Guan, J. Han, M. Chai, and R. Li, “Microplastics in China Sea: Analysis, status, source, and fate,” *Science of The Total Environment*, vol. 803, p. 149887, Jan. 2022, doi: 10.1016/J.SCITOTENV.2021.149887.

[76] V. Nava, M. L. Frezzotti, and B. Leoni, “Raman Spectroscopy for the Analysis of Microplastics in Aquatic Systems,” *https://doi.org/10.1177/00037028211043119*, vol. 75, no. 11, pp. 1341–1357, Sep. 2021, doi: 10.1177/00037028211043119.

[77] M. Becucci, M. Mancini, R. Campo, and E. Paris, “Microplastics in the Florence wastewater treatment plant studied by a continuous sampling method and Raman spectroscopy: A

preliminary investigation," *Science of The Total Environment*, vol. 808, p. 152025, Feb. 2022, doi: 10.1016/J.SCITOTENV.2021.152025.

[78] N. Oveisy, M. Rafiee, A. Rahmatpour, A. S. Nejad, M. Hashemi, and A. Eslami, "Occurrence, identification, and discharge of microplastics from effluent and sludge of the largest WWTP in Iran—South of Tehran," *Water Environment Research*, vol. 94, no. 8, p. e10765, Aug. 2022, doi: 10.1002/WER.10765.

[79] E. A. Ben-David *et al.*, "Microplastic distributions in a domestic wastewater treatment plant: Removal efficiency, seasonal variation and influence of sampling technique," *Science of The Total Environment*, vol. 752, p. 141880, Jan. 2021, doi: 10.1016/J.SCITOTENV.2020.141880.

[80] L. F. Amato-Lourenço, R. Carvalho-Oliveira, G. R. Júnior, L. dos Santos Galvão, R. A. Ando, and T. Mauad, "Presence of airborne microplastics in human lung tissue," *J Hazard Mater*, vol. 416, p. 126124, Aug. 2021, doi: 10.1016/J.JHAZMAT.2021.126124.

[81] A. Ragusa *et al.*, "Plasticenta: First evidence of microplastics in human placenta," *Environ Int*, vol. 146, p. 106274, Jan. 2021, doi: 10.1016/J.ENVINT.2020.106274.

[82] I. K. Clere *et al.*, "Quantification and characterization of microplastics in commercial fish from southern New Zealand," *Mar Pollut Bull*, vol. 184, p. 114121, Nov. 2022, doi: 10.1016/J.MARPOLBUL.2022.114121.

[83] M. Mistri, A. A. Sfriso, E. Casoni, M. Nicoli, C. Vaccaro, and C. Munari, "Microplastic accumulation in commercial fish from the Adriatic Sea," *Mar Pollut Bull*, vol. 174, p. 113279, Jan. 2022, doi: 10.1016/J.MARPOLBUL.2021.113279.

[84] Z. Yan, Y. Liu, T. Zhang, F. Zhang, H. Ren, and Y. Zhang, "Analysis of Microplastics in Human Feces Reveals a Correlation between Fecal Microplastics and Inflammatory Bowel

Disease Status," *Environ Sci Technol*, vol. 56, no. 1, pp. 414–421, Jan. 2022, doi: 10.1021/ACS.EST.1C03924/ASSET/IMAGES/LARGE/ES1C03924_0006.JPEG.

[85] S. Gündoğdu, "Contamination of table salts from Turkey with microplastics," *https://doi.org/10.1080/19440049.2018.1447694*, vol. 35, no. 5, pp. 1006–1014, May 2018, doi: 10.1080/19440049.2018.1447694.

[86] N. A. Yaranal, S. Subbiah, and K. Mohanty, "Identification, extraction of microplastics from edible salts and its removal from contaminated seawater," *Environ Technol Innov*, vol. 21, p. 101253, Feb. 2021, doi: 10.1016/J.ETI.2020.101253.

[87] C. Marina-Montes *et al.*, "Characterization of atmospheric aerosols in the Antarctic region using Raman Spectroscopy and Scanning Electron Microscopy," *Spectrochim Acta A Mol Biomol Spectrosc*, vol. 266, p. 120452, Feb. 2022, doi: 10.1016/J.SAA.2021.120452.

[88] M. J. Nematollahi, B. Keshavarzi, F. Mohit, F. Moore, and R. Busquets, "Microplastic occurrence in urban and industrial soils of Ahvaz metropolis: A city with a sustained record of air pollution," *Science of The Total Environment*, vol. 819, p. 152051, May 2022, doi: 10.1016/J.SCITOTENV.2021.152051.

[89] J. N. Möller *et al.*, "Tackling the Challenge of Extracting Microplastics from Soils: A Protocol to Purify Soil Samples for Spectroscopic Analysis," *Environ Toxicol Chem*, vol. 41, no. 4, pp. 844–857, Apr. 2022, doi: 10.1002/ETC.5024.

[90] Y. Yao, M. Glamoclija, A. Murphy, and Y. Gao, "Characterization of microplastics in indoor and ambient air in northern New Jersey," *Environ Res*, vol. 207, p. 112142, May 2022, doi: 10.1016/J.ENVRES.2021.112142.

[91] G. ElMasry, M. Kamruzzaman, D. W. Sun, and P. Allen, "Principles and Applications of Hyperspectral Imaging in Quality Evaluation of Agro-Food Products: A Review,"

https://doi.org/10.1080/10408398.2010.543495, vol. 52, no. 11, pp. 999–1023, Nov. 2012, doi: 10.1080/10408398.2010.543495.

[92] L. Nigamatzyanova and R. Fakhrullin, "Dark-field hyperspectral microscopy for label-free microplastics and nanoplastics detection and identification in vivo: A Caenorhabditis elegans study," *Environmental Pollution*, vol. 271, p. 116337, Feb. 2021, doi: 10.1016/J.ENVPOL.2020.116337.

[93] J. shan, J. Zhao, L. Liu, Y. Zhang, X. Wang, and F. Wu, "A novel way to rapidly monitor microplastics in soil by hyperspectral imaging technology and chemometrics," *Environmental Pollution*, vol. 238, pp. 121–129, Jul. 2018, doi: 10.1016/J.ENVPOL.2018.03.026.

[94] L. Feld, V. H. da Silva, F. Murphy, N. B. Hartmann, and J. Strand, "A Study of Microplastic Particles in Danish Tap Water," *Water 2021, Vol. 13, Page 2097*, vol. 13, no. 15, p. 2097, Jul. 2021, doi: 10.3390/W13152097.

[95] J. Shan, J. Zhao, Y. Zhang, L. Liu, F. Wu, and X. Wang, "Simple and rapid detection of microplastics in seawater using hyperspectral imaging technology," *Anal Chim Acta*, vol. 1050, pp. 161–168, Mar. 2019, doi: 10.1016/J.ACA.2018.11.008.

[96] N. B. Nguyen, M. K. Kim, Q. T. Le, D. N. Ngo, K. D. Zoh, and S. W. Joo, "Spectroscopic analysis of microplastic contaminants in an urban wastewater treatment plant from Seoul, South Korea," *Chemosphere*, vol. 263, p. 127812, Jan. 2021, doi: 10.1016/J.CHEMOSPHERE.2020.127812.

[97] C. Vidal and C. Pasquini, "A comprehensive and fast microplastics identification based on near-infrared hyperspectral imaging (HSI-NIR) and chemometrics," *Environmental Pollution*, vol. 285, p. 117251, Sep. 2021, doi: 10.1016/J.ENVPOL.2021.117251.

[98] Y. Zhang *et al.*, "Hyperspectral Imaging Based Method for Rapid Detection of Microplastics in the Intestinal Tracts of Fish," *Environ Sci Technol*, vol. 53, no. 9, pp. 5151–5158, May 2019, doi: 10.1021/ACS.EST.8B07321/ASSET/IMAGES/LARGE/ES-2018-073219_0004.JPEG.

[99] H. Huang *et al.*, "Underwater hyperspectral imaging for in situ underwater microplastic detection," *Science of The Total Environment*, vol. 776, p. 145960, Jul. 2021, doi: 10.1016/J.SCITOTENV.2021.145960.

[100] M. Pollard, E. Hunsicker, and M. Platt, "A Tunable Three-Dimensional Printed Microfluidic Resistive Pulse Sensor for the Characterization of Algae and Microplastics," *ACS Sens*, vol. 5, no. 8, pp. 2578–2586, Aug. 2020, doi: 10.1021/ACSSENSORS.0C00987/ASSET/IMAGES/LARGE/SE0C00987_0007.JPEG.

[101] C. Honrado, P. Bisegna, N. S. Swami, and F. Caselli, "Single-cell microfluidic impedance cytometry: from raw signals to cell phenotypes using data analytics," *Lab Chip*, vol. 21, no. 1, pp. 22–54, 2021, doi: 10.1039/D0LC00840K.

[102] K. Cheung, S. Gawad, and P. Renaud, "Impedance spectroscopy flow cytometry: On-chip label-free cell differentiation," *Cytometry Part A*, vol. 65A, no. 2, pp. 124–132, Jun. 2005, doi: 10.1002/CYTO.A.20141.

[103] B. C. Colson and A. P. M. Michel, "Flow-Through Quantification of Microplastics Using Impedance Spectroscopy," *ACS Sens*, vol. 6, no. 1, pp. 238–244, Jan. 2021, doi: 10.1021/ACSSENSORS.0C02223/ASSET/IMAGES/LARGE/SE0C02223_0005.JPEG.

[104] N. Meyers *et al.*, "Microplastic detection and identification by Nile red staining: Towards a semi-automated, cost- and time-effective technique," *Science of The Total Environment*, vol. 823, p. 153441, Jun. 2022, doi: 10.1016/J.SCITOTENV.2022.153441.

[105] A. Käppler *et al.*, "Comparison of μ-ATR-FTIR spectroscopy and py-GCMS as identification tools for microplastic particles and fibers isolated from river sediments," *Anal Bioanal Chem*, vol. 410, no. 21, pp. 5313–5327, Aug. 2018, doi: 10.1007/S00216-018-1185-5/TABLES/2.

[106] D. Elkhatib and V. Oyanedel-Craver, "A Critical Review of Extraction and Identification Methods of Microplastics in Wastewater and Drinking Water," *Environ Sci Technol*, vol. 54, no. 12, pp. 7037–7049, Jun. 2020, doi: 10.1021/ACS.EST.9B06672/SUPPL_FILE/ES9B06672_SI_001.PDF.

[107] Z. Chen, W. Wei, X. Liu, and B. J. Ni, "Emerging electrochemical techniques for identifying and removing micro/nanoplastics in urban waters," *Water Res*, vol. 221, p. 118846, Aug. 2022, doi: 10.1016/J.WATRES.2022.118846.

[108] C. Clausen *et al.*, "Bacteria Detection and Differentiation Using Impedance Flow Cytometry," *Sensors*, vol. 18, no. 10, p. 3496, 2018, doi: 10.3390/s18103496.

[109] C. Bernabini, D. Holmes, and H. Morgan, "Micro-impedance cytometry for detection and analysis of micron-sized particles and bacteria," *Lab Chip*, vol. 11, no. 3, pp. 407–412, Feb. 2011, doi: 10.1039/C0LC00099J.

[110] T. Sun, C. van Berkel, N. G. Green, and H. Morgan, "Digital signal processing methods for impedance microfluidic cytometry," *Microfluid Nanofluidics*, vol. 6, no. 2, pp. 179–187, Jun. 2009, doi: 10.1007/S10404-008-0315-3/FIGURES/8.

[111] M. Evander, A. J. Ricco, J. Morser, G. T. A. Kovacs, L. L. K. Leung, and L. Giovangrandi, "Microfluidic impedance cytometer for platelet analysis," *Lab Chip*, vol. 13, no. 4, pp. 722–729, Jan. 2013, doi: 10.1039/C2LC40896A.

[112] S. Zhu, X. Zhang, Z. Zhou, Y. Han, N. Xiang, and Z. Ni, “Microfluidic impedance cytometry for single-cell sensing: Review on electrode configurations,” *Talanta*, vol. 233, p. 122571, Oct. 2021, doi: 10.1016/J.TALANTA.2021.122571.

[113] S. Gawad, L. Schild, and P. Renaud, “Micromachined impedance spectroscopy flow cytometer for cell analysis and particle sizing,” *Lab Chip*, vol. 1, no. 1, pp. 76–82, Jan. 2001, doi: 10.1039/B103933B.

[114] D. Tang, M. Chen, Y. Han, N. Xiang, and Z. Ni, “Asymmetric serpentine microchannel based impedance cytometer enabling consistent transit and accurate characterization of tumor cells and blood cells,” *Sens Actuators B Chem*, vol. 336, p. 129719, Jun. 2021, doi: 10.1016/J.SNB.2021.129719.

[115] C. Petchakup, P. E. Hutchinson, H. M. Tay, S. Y. Leong, K. H. H. Li, and H. W. Hou, “Label-free quantitative lymphocyte activation profiling using microfluidic impedance cytometry,” *Sens Actuators B Chem*, vol. 339, p. 129864, Jul. 2021, doi: 10.1016/J.SNB.2021.129864.

[116] S. Yan and D. Yuan, “Continuous microfluidic 3D focusing enabling microflow cytometry for single-cell analysis,” *Talanta*, vol. 221, p. 121401, Jan. 2021, doi: 10.1016/J.TALANTA.2020.121401.

[117] F. Caselli, A. de Ninno, R. Reale, L. Businaro, and P. Bisegna, “A Bayesian Approach for Coincidence Resolution in Microfluidic Impedance Cytometry,” *IEEE Trans Biomed Eng*, vol. 68, no. 1, pp. 340–349, Jan. 2021, doi: 10.1109/TBME.2020.2995364.

[118] G. Mernier, E. Duqi, and P. Renaud, “Characterization of a novel impedance cytometer design and its integration with lateral focusing by dielectrophoresis,” *Lab Chip*, vol. 12, no. 21, pp. 4344–4349, Oct. 2012, doi: 10.1039/C2LC40551B.

[119] K. Makino, N. Yamamoto, K. Higuchi, N. Harada, H. Ohshima, and H. Terada, “Phagocytic uptake of polystyrene microspheres by alveolar macrophages: effects of the size and surface properties of the microspheres,” *Colloids Surf B Biointerfaces*, vol. 27, no. 1, pp. 33–39, Jan. 2003, doi: 10.1016/S0927-7765(02)00042-5.

[120] Y. Yan, J. Luo, D. Guo, and S. Wen, “Dynamic Dielectrophoresis Model of Multi-Phase Ionic Fluids,” *PLoS One*, vol. 10, no. 2, p. e0117456, Feb. 2015, doi: 10.1371/JOURNAL.PONE.0117456.

[121] B. P. Cahill Brian Cahill, “Optimization of an impedance sensor for droplet-based microfluidic systems,” *https://doi.org/10.1117/12.886887*, vol. 8066, no. 5, pp. 133–140, May 2011, doi: 10.1117/12.886887.

[122] E. W. M. Kemna, L. I. Segerink, F. Wolbers, I. Vermes, and A. van den Berg, “Label-free, high-throughput, electrical detection of cells in droplets.,” *undefined*, vol. 138, no. 16, pp. 4585–4592, Aug. 2013, doi: 10.1039/C3AN00569K.